JAMES | Journal of Advances in Modeling Earth Systems®

RESEARCH ARTICLE
10.1029/2025MS005462

Balancing Backscatter and Diffusion in a 1/4° Forced Global Ocean Model

H. Yassin[1], G. Marques[2], and I. Grooms[1]

[1]Department of Applied Mathematics, University of Colorado, Boulder, CO, USA, [2]Climate and Global Dynamics Laboratory, National Center for Atmospheric Research, Boulder, CO, USA

Key Points:

- Negative viscosity backscatter in quarter degree models consistently drives overly strong poleward heat transport
- Poleward heat transport differences mainly reflect where backscatter acts especially whether it is applied in the Southern Ocean
- A resolution function that applies diffusion where eddies are unresolved and backscatter elsewhere can help balance energy and transport

Correspondence to:
H. Yassin,
hoya8459@colorado.edu

Citation:
Yassin, H., Marques, G., & Grooms, I. (2026). Balancing backscatter and diffusion in a 1/4° forced global ocean model. *Journal of Advances in Modeling Earth Systems*, *18*, e2025MS005462. https://doi.org/10.1029/2025MS005462

Received 26 AUG 2025
Accepted 24 FEB 2026

Abstract Mesoscale ocean eddies in 1/4° global ocean models lie near the grid scale and are overdamped by viscosity, leading to reduced eddy kinetic energy, weak sea surface height variability, and mean-state biases. Backscatter has been proposed to remedy this problem by re-injecting dissipated energy, but its diabatic consequences are poorly characterized. We first show that using backscatter alone in a 1/4° forced CESM2-MOM6 ocean–sea ice model produces unrealistically large southward heat transport. To address this problem, we define a non-dimensional ratio $R = L_d/\Delta$ (deformation radius over grid spacing) and adopt a nearly step-like resolution function with a threshold of $R_0 = 0.5$. Isopycnal height and tracer diffusion act where $R < 0.5$ and backscatter acts where $R > 0.5$. We compare two backscatter schemes that differ mainly in where they apply backscatter. One applies backscatter broadly in the Southern Ocean, whereas the other confines it near western boundary currents. Both schemes energize the model by 20%–25%. When backscatter is applied in the Southern Ocean, it energizes and barotropizes the flow but also increases southward heat transport, warms surface temperatures, shifts deep winter mixed layers poleward, and reduces Antarctic sea ice. In contrast, limiting backscatter to western boundary currents strongly enhances eddy kinetic energy there while keeping Southern Ocean heat transport, sea surface temperatures, mixed-layer depth, and sea ice much closer to the reference run. These results show strong sensitivity to backscatter placement and, in this configuration, favor confining it to western boundary currents.

Plain Language Summary Ocean eddies move heat and nutrients around the globe and shape Earth's climate. Many global climate models now use a quarter-degree grid spacing, where ocean eddies are only partly resolved. At this resolution, older smoothing methods designed to mimic unrepresented eddies now remove too much energy and either eliminate the eddies or make them too weak. One proposed fix is backscatter, which returns some of that lost energy to the flow. We test backscatter in a global ocean–sea ice model and find that simply turning it on everywhere results in excessive heat transport toward the Southern Ocean. We then introduce a simple rule that determines where to smooth eddies and where to return energy, based on how large the eddies are relative to the grid. We test two ways of applying backscatter and find that the model is sensitive to where it is active. Energizing the Southern Ocean increases heat transport, whereas focusing backscatter on western boundary currents mainly strengthens those currents while leaving large-scale Southern Ocean patterns closer to the reference simulation. These findings emphasize the need to understand how backscatter affects heat transport in realistic global ocean models.

1. Introduction

Coarse resolution ocean models (with a grid spacing of $\sim 1°$ or coarser) fail to resolve mesoscale ocean eddies nearly everywhere and so must parameterize their effects through the use of isopycnal height diffusion and along-isopycnal tracer diffusion (Gent & McWilliams, 1990; Redi, 1982; Solomon, 1971). Isopycnal height diffusion prescribes a downgradient diffusion of isopycnal layer height, emulating the extraction of available potential energy by mesoscale eddies, whereas isopycnal tracer diffusion represents the lateral stirring of heat and salinity along isopycnals. As the grid spacing is refined to 1/4°, the model enters a "gray zone" in which mesoscale eddies begin to appear, yet remain too poorly resolved to reproduce eddy effects that parameterizations represent in coarse resolution models. In this partially resolved regime, however, even a modest amount of isopycnal height diffusion smooths away baroclinic eddies, damping mesoscale variability and sea surface height variance. Moreover, even without applying height diffusion, these marginally resolved eddies lie close to the grid scale and are therefore strongly dissipated by the model's viscosity, which is required for numerical stability.

1.1. Parameterizations in the Gray Zone

Various approaches have been proposed to address the challenges of parameterizing mesoscale eddies in the "gray zone." One approach confines isopycnal height diffusion to areas where the grid is too coarse to resolve eddies (Hallberg, 2013). To accomplish this, the isopycnal height diffusivity is multiplied by a resolution function that scales the diffusivity to zero once the grid spacing is sufficiently small. Instead of a diffusivity that tapers smoothly to zero, Hallberg (2013) recommends a step-function that abruptly switches off isopycnal height diffusion once eddy transports become resolved—avoiding the problematic partial parameterization where non-zero diffusivities smooth away eddies without reproducing the associated eddy-driven transports. Although this approach confines baroclinic damping to regions where eddies remain unresolved, it does not prevent the excessive dissipation of marginally resolved eddies by the model's viscosity elsewhere.

This overdissipation of marginally resolved eddies by viscosity can be mitigated by introducing backscatter. Although viscous closures are intended to prevent the accumulation of enstrophy at the grid scale, they also dissipate a significant amount of kinetic energy that, in the real ocean, would cascade to larger scales. A closely related problem and remedy have been recognized earlier in atmospheric models (Berner et al., 2009; Shutts, 2005). To counteract this excessive dissipation of marginally resolved eddies, Jansen and Held (2014) introduce, as a novel ocean implementation, a Laplacian anti-viscosity term in the horizontal momentum equation to return a portion of the dissipated energy to the resolved flow. Combining biharmonic viscosity with a Laplacian anti-viscosity still dissipates enstrophy at the grid scale while backscattering part of the lost energy to resolved scales. Originally introduced in a two-layer quasigeostrophic setting, backscatter has subsequently been implemented in more realistic primitive equation models (Jansen et al., 2015), with the backscatter strength determined by a local, vertically-integrated prognostic budget for subgrid-scale kinetic energy. In an idealized two-layer primitive equation model, the scheme increases eddy kinetic energy and improves eddy-driven transport even in regimes where the deformation radius is close to the grid spacing. Yet the scheme relies on the presence of eddies. If no eddies form, the flow remains nearly laminar with weak velocity gradients. Because viscous closures act mainly on strong gradients, the resulting viscous dissipation is small, and consequently, there is little kinetic energy available to backscatter. As a result, in coarser resolution idealized models, backscatter has limited impact.

Building on this approach, Juricke et al. (2019) develop a backscatter scheme for unstructured-grid ocean models that uses a three-dimensional subgrid-scale kinetic energy budget and applies a depth-dependent backscatter. Juricke, Danilov, Koldunov, Oliver, Sein, et al. (2020) next propose a simpler "kinematic" variant: rather than prognostically tracking a subgrid-scale kinetic energy reservoir in each vertical column, their scheme computes a negative viscosity at each level (smoothed through cell-vertex averaging) so it can immediately re-inject part of the lost energy. More recently, Bagaeva et al. (2024) extend the original dynamic framework by adding subgrid-energy advection and stochastic forcing. In contrast, Grooms (2023) introduces the Leith + E backscatter scheme, which embeds backscatter within a Leith-like closure by prescribing that a fixed fraction of the kinetic energy dissipated by biharmonic viscosity is returned to larger scales, while maintaining scale separation and adjustable net dissipation. As in Juricke, Danilov, Koldunov, Oliver, Sein, et al. (2020), the anti-viscosity in the Leith + E backscatter scheme is computed independently at each vertical level, enabling the scheme to respond to depth-varying flow structures and dissipation rates.

Rather than setting backscatter amplitude solely from viscous dissipation, a physically motivated alternative is to tie it to the available potential energy dissipated by isopycnal height diffusion. Both Jansen et al. (2019) and Bachman (2019) adopt this strategy. In Jansen et al. (2019), the lost available potential energy enters the vertically integrated subgrid-scale kinetic energy budget as an additional source term, enabling backscatter to compensate for energy removed by isopycnal height diffusion. A smooth resolution function then modulates both isopycnal height diffusion and backscatter, switching them off in regions where the grid spacing is fine enough to resolve eddies. Jansen et al. (2019) show that this strategy avoids the problematic partial parameterization problem suffered when a smooth resolution function is used with isopycnal height diffusion alone. Tested in an adiabatic, six-layer NeverWorld primitive equation configuration idealizing the Southern Hemisphere, this scheme outperforms a simple step-function isopycnal height diffusion approach by preserving more eddy variability and kinetic energy. Meanwhile, Bachman (2019) develops a related GM + E closure that also couples the diffusive sink of available potential energy to a backscatter term; however, unlike Jansen et al. (2019), this approach does not employ an explicit subgrid kinetic energy budget to set the backscatter coefficient. Instead, it balances the implied available potential energy dissipation by instantaneously injecting an equivalent amount of kinetic energy

back into the resolved flow. Extending this framework, Grooms et al. (2025) introduce a stochastic GM + E variant that backscatters a prescribed fraction of the energy lost due to isopycnal height diffusion as random velocity increments, markedly increasing variability in coarse, non-eddying ocean models.

Although the Jansen et al. (2019) scheme's combination of isopycnal height diffusion with backscatter improves the simulation relative to one using a step-function isopycnal height diffusion alone, it still produces less kinetic energy than an unparameterized run that relies only on hyperviscous dissipation—which is itself already over-dissipative. In response to this, Yankovsky et al. (2024) argue that when eddies are marginally resolved, using backscatter alone might be preferable. Through systematic experimentation in the idealized adiabatic Neverworld2 configuration (Marques et al., 2022), Yankovsky et al. (2024) demonstrate that accurately matching both the kinetic energy and available potential energy of a high-resolution benchmark requires not only adjusting the amplitude of backscatter, but also tuning its vertical structure. They find that backscatter can recover either the kinetic energy or the available potential energy—but not both—unless the re-injected energy is surface-intensified and minimized near the bottom boundary. Energy injected too deep is rapidly lost to bottom drag, while uniform vertical structures remove too much available potential energy at depth by excessively flattening isopycnals. By imposing a surface-intensified structure on the Laplacian ant-viscosity coefficient, they achieve a configuration that restores both kinetic energy and available potential energy to levels nearly identical to the high-resolution reference case. The vertical structure advocated by Yankovsky et al. (2024), however, is not the only option. Zhang et al. (2024) notes that smaller eddies decay more rapidly with depth. Therefore, they advocate for a scale-aware vertical structure based on surface quasigeostrophic theory rather than the scale-agnostic vertical structure advocated by Yankovsky et al. (2024). In practice, these vertical structure prescriptions only apply to schemes like Jansen et al. (2019) that use a vertically-integrated subgrid-scale budget and therefore require an assumed vertical profile. Other formulationse "dynamic" backscatter (Juricke, Danilov, Koldunov, Oliver, & Sidorenko, 2020), the "kinematic" backscatter (Juricke, Danilov, Koldunov, Oliver, Sein, et al., 2020), or the Leith + E backscatter (Grooms, 2023), compute the anti-viscosity at each vertical level and thus require no additional prescription.

1.2. Performance in Forced Global Ocean–Sea Ice Models

In global eddy-permitting (nominal 1/4°) forced ocean–sea ice models, three negative-viscosity backscatter variants have been documented so far. Two such backscatter schemes have been implemented in FESOM2 (Danilov et al., 2017), in a 1/4° configuration with 46 vertical layers, driven by CORE-II atmospheric fields (Large & Yeager, 2009). In FESOM2, the tested schemes are the "dynamic" backscatter approach using a three-dimensional subgrid-scale kinetic energy budget (Juricke, Danilov, Koldunov, Oliver, & Sidorenko, 2020) and the "kinematic" backscatter approach (Juricke, Danilov, Koldunov, Oliver, Sein, et al., 2020) which forgoes an explicit subgrid-scale kinetic energy budget and instantaneously re-injects part of the dissipated energy. Because the results from the "dynamic" variant are more fully documented, we focus on it below. In that investigation, neither the control nor the backscatter simulations use any isopycnal height diffusion, though both use an isopycnal tracer diffusivity of 3000 $m^2 s^{-1}$ that is locally scaled relative to the 1° grid spacing at the equator. Aside from FESOM2, backscatter has also been tested in OM4 (Adcroft et al., 2019), where Chang et al. (2023) implement the Jansen et al. (2019) backscatter scheme. OM4 uses a nominal 1/4° horizontal grid spacing and 75 vertical layers and is forced with JRA55-do v1.4.0 atmospheric fields (Tsujino et al., 2018). In this configuration, isopycnal tracer diffusion is not applied. The Jansen et al. (2019) backscatter scheme uses a depth-integrated subgrid-scale kinetic energy budget with depth-independent backscatter coefficient. Although the original implementation of the Jansen et al. (2019) backscatter scheme consists of applying both isopycnal height diffusion and backscatter at the same locations scaled by a smooth resolution function, Chang et al. (2023) turn off the isopycnal height diffusion so that the scheme consists solely of backscatter multiplied by a resolution function that scales the backscatter to zero where eddies are resolved. Consequently, all published backscatter results in 1/4° ocean–sea ice models employ backscatter in isolation without isopycnal height diffusion.

In both FESOM2 and OM4, backscatter energizes resolved flows that would otherwise be excessively damped, increasing eddy kinetic energy and sea surface height variability toward observed values. In FESOM2, this energization reduces biases in sea surface height, temperature, and salinity, and mitigates a long-standing North Atlantic sea surface temperature dipole consisting of a warm bias along the eastern US coast and a cold bias associated with an insufficient northward extension of the North Atlantic Current. In OM4, backscatter likewise increases eddy activity and variability as shown by Chang et al. (2023), whose analysis is primarily focused on the

North Atlantic. They show that reducing the warm bias along the eastern US coast is achieved by applying backscatter further north near the Flemish Cap; here the remote energization of deep currents facilitates more realistic Gulf Stream separation, while local energization in the Flemish Cap region helps to shift the North Atlantic Current northward, thereby reducing the cold bias.

In addition to enhancing eddy kinetic energy and reducing biases, backscatter also alters key dynamical features such as mixed-layer depth and the position of surface currents. In FESOM2, backscatter modifies mixed-layer depths, with the largest changes occurring in locations where the mixed layer is already deep. A tripole pattern of shoaling surrounded by deepening is found near western boundary currents (also seen in OM4 in the North Atlantic). In the Labrador Sea, FESOM2 shows mixed-layers shoaling everywhere except immediately south of Greenland, whereas OM4 exhibits deepening there. In FESOM2, mixed layers also shoal on the Antarctic continental shelf, and, in the Southern Ocean, mixed layers deepen and shoal corresponding to the shifting position of the Antarctic Circumpolar Current. These shifts in the circumpolar current help correct a bias in sea surface height variability in FESOM2. OM4 also exhibits meridional shifts in Southern Ocean currents, but these shifts do not always reduce model biases.

Backscatter also causes a broad warming of the Southern Ocean, increasing sea surface temperatures. In FESOM2, this warming reduces existing sea surface temperature biases, whereas in OM4 it exacerbates them. Part of the sea surface temperature response stems from meridional shifts in surface currents, and parts stem from increased southward heat transport by energized eddies. The stronger Southern Ocean eddies are more effective at flattening isopycnal slopes, weakening the upper cell of the Atlantic Meridional Overturning Circulation (Juricke, Danilov, Koldunov, Oliver, & Sidorenko, 2020)—though OM4 also shows a strengthening between 20°–40°N—and increasing the strength of the lower cell. In FESOM2, the increased heat transport leads to unrealistically small sea ice extent and thinner sea ice.

1.3. Outline

Motivated by the success of backscatter-only parameterizations in marginally resolved ocean models, we initially compare two such schemes in CESM2-MOM6: the Jansen et al. (2019) scheme (with isopycnal height diffusion disabled), and the Leith + E scheme (Grooms, 2023). However, in Section 2, we find that the backscatter-only runs produce unrealistically large heat transports and large, recurring Weddell Sea polynyas. To remedy this, we devised a hybrid approach in which isopycnal height and tracer diffusion are applied wherever the non-dimensional number, $R = L_d/\Delta$ (where L_d is the deformation radius and Δ the grid spacing), falls below a threshold R_0, and backscatter is used otherwise. Guided by results from idealized models (Section 2.3), we select a threshold of $R_0 = 0.5$ (the thin black contour shown in Figure 1), implying that diffusion is applied wherever there are fewer than half a grid cell per deformation radius ($R < 0.5$) and backscatter otherwise ($R > 0.5$). Using this hybrid approach, we perform four 61-year simulations: a reference simulation, a diffusion-only run where isopycnal height and tracer diffusion are applied where $R < 0.5$, and two hybrid runs combining isopycnal height and tracer diffusion where $R < 0.5$ with either the Jansen et al. (2019) or Leith + E backscatter where $R > 0.5$.

In Section 3, we present the results of these experiments. In regions exposed to isopycnal height and tracer diffusion, mean currents weaken and isopycnal slopes flatten. However, applying isopycnal height and tracer diffusion in a nearly discontinuous manner has unexpected consequences. Namely, it strengthens currents and steepens isopycnal slopes in regions where the parameterizations are not being applied, even in simulations with no backscatter. Where backscatter is active, both hybrid runs energize western boundary currents and their extensions, especially amplifying their eddy component. Yet, only the Jansen et al. (2019) scheme results in a broad energization and barotropization of the Southern Ocean. This energization, however, is at the expense of excessive poleward heat transport, a southward shift in the band of deep Southern Ocean mixed layers, and pronounced loss of sea ice. In contrast, the Leith + E scheme confines energy injection primarily to western boundary currents with smaller impact on the Southern Ocean. This contrast reflects where each scheme applies backscatter. The Jansen et al. (2019) scheme, with its vertically-integrated subgrid-scale kinetic energy budget, spreads anti-viscosity widely while the Leith + E closure returns energy mainly in high eddy activity regions. This comparison indicates a practical preference, in this configuration, for avoiding broad application of backscatter in the Southern Ocean. For completeness, we also provide an Appendix A that compares the sea surface height in the four simulations with satellite altimetry.

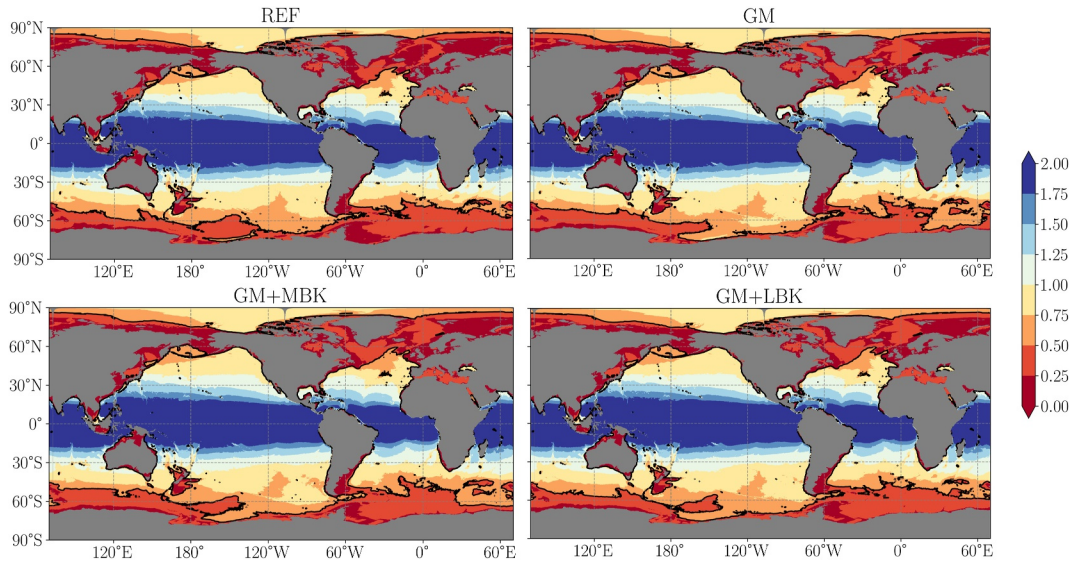

Figure 1. Time-mean of the deformation radius to grid spacing ratio, $R = L_d/\Delta$, averaged over the final 30 years of each simulation. The simulations are: REF (reference); GM (isopycnal height and tracer diffusion only where $R < 0.5$); GM + MBK (isopycnal height and tracer diffusion where $R < 0.5$, and Jansen et al. (2019) backscatter scheme where $R > 0.5$); and GM + LBK (isopycnal height and tracer diffusion where $R < 0.5$, and Leith + E backscatter where $R > 0.5$). The black contour marks the threshold $R_0 = 0.5$ in the step-function resolution mask defined in Equation 2.

In Section 4, we discuss these results. We begin by examining the fidelity of backscatter closures in reproducing eddy effects. Then we evaluate the appropriateness of the chosen $R = 0.5$ threshold and explore more general strategies for combining isopycnal height diffusion with backscatter. Finally, we emphasize the need to understand and quantify the diabatic impacts of backscatter in realistic global ocean models.

2. Model Development

2.1. Numerical Model

We use the Community Earth System Model 2 (Danabasoglu et al., 2020) global configuration of the Modular Ocean Model (MOM6) with a nominal $1/4°$ horizontal grid spacing and a hybrid z^* vertical coordinate with 75 vertical levels (similar to Adcroft et al. (2019)). The model uses MOM6's vertical Lagrangian dynamical core (Griffies et al., 2020) coupled to the CICE5 sea ice model (Hunke et al., 2015). Surface boundary layer mixing is represented with the K-profile parameterization (Large et al., 1994), and mixed-layer restratification by submesoscale eddies follows Fox-Kemper et al. (2011).

The backscatter scheme is implemented in the horizontal momentum equation, which can be written as

$$\partial_t \mathbf{u}(x,y,z) = \cdots - \nabla \cdot \left[\nu_2(x,y,z)\,\nabla \mathbf{u}(x,y,z)\right] - \nabla \cdot \left[\nu_4(x,y,z)\,\nabla \nabla^2 \mathbf{u}(x,y,z)\right], \quad (1)$$

where $\mathbf{u}$ is the horizontal velocity, ν_2 is the Laplacian viscosity, ν_4 is the biharmonic viscosity, and $\cdots$ indicates other standard terms in the momentum equation, which we leave fixed (the time-dependence in the above equation has been suppressed). Whereas the prognostic Jansen et al. (2019) backscatter scheme applies the negative viscosity to the raw horizontal velocity $\mathbf{u}$ (as shown in Equation 1), the instantaneous Leith + E scheme applies it to the smoothed horizontal velocity, $\overline{\mathbf{u}}$, where the overline denotes a low-pass spatial filter.

Our objective is to compare two schemes. The first is the Jansen et al. (2019) scheme, which uses a vertically integrated subgrid-scale kinetic energy budget. We disable the co-located isopycnal height diffusion as in Chang et al. (2023) and use an equivalent barotropic squared vertical structure as recommended by Yankovsky et al. (2024). The second scheme is the Leith + E backscatter scheme (Grooms, 2023), which computes a local negative viscosity from the forward enstrophy cascade and instantaneously re-injects energy without an explicit kinetic energy budget. The Leith + E backscatter simulation using a Leith-like biharmonic viscosity whereas all

other simulations use the Smagorinsky-like form of Griffies and Hallberg (2000) for ν_4 with a coefficient of $c_{\text{smag}} = 0.06$. All simulations use a latitudinally-dependent background biharmonic viscosity of the form $u_4\Delta^3$ where $u_4 = 0.01\,\text{m}\,\text{s}^{-1}$ and Δ is the local grid spacing.

2.2. The Need for Isopycnal Height Diffusion

The first question we addressed was whether we should use isopycnal height diffusion with backscatter. However, the success of the backscatter-only runs in global forced ocean–sea ice models (Chang et al., 2023; Juricke, Danilov, Koldunov, Oliver, Sein, et al., 2020; Juricke, Danilov, Koldunov, Oliver, & Sidorenko, 2020) and the ability of backscsatter alone to energize eddies and extract available potential energy from the mean flow in idealized adiabatic models (Yankovsky et al., 2024) convinced us to focus initially on backscatter-only configurations.

This focus on backscatter-only schemes, however, revealed a major flaw: despite energizing the flow, enhancing eddy activity, and reducing the North Atlantic temperature bias, the schemes also produced a very large spurious polynya in the Weddell Sea: it appeared by year 6 under the Leith + E scheme and year 10 under the Jansen et al. (2019) scheme. In each case, the polynya reappeared every Southern Hemisphere winter, expanded annually, and was accompanied by widespread Southern Ocean warming and a pronounced increase in southward heat transport. The formation of this spurious polynya is not unique to backscatter. As noted above, our model biharmonic viscosity is taken to be the maximum of a dynamical Smagorinsky or Leith viscosity and a fixed background biharmonic viscosity $u_4\Delta^3$ where $u_4 = 0.01\,\text{m}\,\text{s}^{-1}$ and Δ is the local grid spacing. When we reduced u_4 by a factor of 10, in a simulation without any backscatter, we found a similar polynya and heat transport spike. Moreover, other global backscatter studies have observed similar Southern Ocean warming or unrealistic reductions in sea ice (Chang et al., 2023; Juricke, Danilov, Koldunov, Oliver, & Sidorenko, 2020). Together, these results show that a blanket reduction in dissipation allows eddy energy to grow sufficiently to upset the Southern Ocean heat balance and possibly trigger unrealistic phenomena such as recurring polynyas or reduced sea ice. These findings underscore the need to understand the diabatic consequences of enhanced eddy activity that idealized adiabatic simulations have overlooked.

To prevent the formation of this spurious polynya, we first tried tapering backscatter with a resolution function. Unlike Jansen et al. (2019) and Chang et al. (2023), our initial simulations applied backscatter uniformly. We then introduced a step-function tapering based on the ratio $R = L_d/\Delta$, where L_d is the local deformation radius and Δ is the local grid spacing. In one experiment, backscatter was active only where $R < 1$ (high latitudes and continental margins), and in the other, only where $R > 1$ (lower latitudes); neither configuration prevented the formation of Weddell Sea polynyas. The fact that polynyas still form even when backscatter is applied only where $R > 1$ suggests that backscatter alters the heat transport to the Southern Ocean by modifying the meridional overturning circulation. We discuss this mechanism further in Section 3.3.

Because neither approach to tapering backscatter succeeded, we concluded that some explicit restratification was needed (in addition to the submesoscale mixed-layer eddy restratification scheme of Fox-Kemper et al. (2011), which is active in all simulations). We therefore applied isopycnal height diffusion (with an equivalent barotropic vertical structure) in regions with $R < 1$, so that diffusion is present in the Southern Ocean and Weddell Sea, and backscatter in regions where $R > 1$. The $R = 1$ threshold was a provisional testing choice to ensure diffusion covered the Weddell Sea; it was not intended as final. At first, we specified a spatially variable isopycnal height diffusivity using a subgrid-scale kinetic energy budget, but the resulting diffusivity in the Weddell Sea remained too weak to halt polynya growth. When we switched to a constant isopycnal height diffusivity of $1,000\ \text{m}^2\,\text{s}^{-1}$ at the ocean surface, we finally succeeded. This change restratified the upper ocean and arrested the development of spurious Weddell Sea polynyas. The next section provides a method for choosing the resolution function threshold.

2.3. Specifying the Resolution Function

Preventing the spurious Weddell Sea polynya led us combine isopycnal height diffusion and backscatter in a new way. Unlike Jansen et al. (2019), who apply diffusion and backscatter in the same locations, we place them in complementary regions. The key idea is that isopycnal height diffusion is needed where the grid is too coarse to resolve eddies, whereas backscatter is needed where the grid permits eddies but the model over dissipates them.

To avoid the partial parameterization problem described by Hallberg (2013), we use a step-like resolution function of the form

$$r(R) = \begin{cases} 1 & \text{if } R > R_0 \\ 0 & \text{if } R \le R_0 \end{cases}. \tag{2}$$

Selecting the threshold R_0 involves three constraints.

First, we need a lower bound below which isopycnal height diffusion is necessary. In a two-layer primitive equation model, Hallberg (2013) demonstrated that at least two grid points per deformation radius are necessary for resolved eddies to reproduce the overturning they generate at high resolution. When the threshold was lowered to $R_0 = 1$, the resolved transport weakened, and when it was pushed below one the overturning collapsed wherever the diffusion was turned off. Consequently, Hallberg (2013) recommended a threshold of $R_0 = 2$, noting that even higher values might be necessary in configurations with additional vertical modes.

Second, we need a minimum resolution above which backscatter begins to be beneficial, as negative-Laplacian backscatter can only energize existing eddy fluctuations. Using two-layer quasigeostrophic simulations, Jansen and Held (2014) found meaningful improvements from backscatter once the ratio exceeded $R \approx 0.4$; below this threshold, the flow remains laminar. Two-layer primitive equation experiments by Jansen et al. (2015) reproduced this threshold, finding no eddy formation below $R < 0.4$, regardless of the presence of backscatter. Thus the lowest practical threshold at which backscatter becomes helpful is close to the half-grid point mark, $R_0 \approx 0.5$. The fifteen-layer adiabatic primitive equation simulations in the NeverWorld2 configuration by Yankovsky et al. (2024) support this lower bound. Although they found that backscatter effectively energized eddies even at $1/2°$ grid spacing, examining Figure 2 from Marques et al. (2022), which shows the deformation radius to grid spacing ratio for the NeverWorld2 setup, we note that their model Southern Ocean at $1/2°$ corresponds to $R \approx 0.4$–0.6, consistent with the earlier findings.

Third, we need an upper bound above which backscatter is no longer needed because the resolved solution has effectively converged. Both Jansen and Held (2014) and Jansen et al. (2015) show that the benefit of backscatter saturate by about $R = 3$, beyond which hyperviscosity removes negligible energy. However, both of these studies were limited to two vertical layers. Experiments with more vertical structure push this ceiling higher. In a six-layer quasigeostrophic double-gyre model, Grooms (2023) finds that even at $R = 4.5$, the kinetic energy was still 8%–20% below that of a well-resolved $R = 8$ benchmark simulation. At coarser resolutions, the kinetic energy deficit increased further: around 30% at $R = 2$ and about 40% at $R = 1$.

Considering these constraints collectively, we might initially conclude that isopycnal diffusion should be applied where $R \le 2$ and backscatter where $0.5 \le R \le 8$. In a $1/4°$ model, however, using $R < 2$ would place every major extratropical current and the entire Southern Ocean under isopycnal height diffusion, smoothing away nearly all baroclinic eddies, while backscatter would be confined to a $\pm 20°$ equatorial band (corresponding to the dark blue region in all panels of Figure 1). Because our goal is to produce a more energetic simulation than a reference with hyperviscosity alone, we cannot allow isopycnal height diffusion to dominate such a large part of the world ocean. Moreover, although Hallberg (2013) recommends that isopycnal height diffusion should be applied for $R < 2$ to capture eddy transports, this recommendation does not account for the potential use of backscatter to energize partially resolved eddies. Taking this into account, we instead choose to apply isopycnal height diffusion where $R < 0.5$, and backscatter between $0.5 \le R \le 8$. In practice, the ratio $R = L_d/\Delta$ reaches a maximum of approximately 6.5 at the equator, meaning that the model remains over-dissipative everywhere. Therefore, our practical criterion simplifies to applying isopycnal height diffusion for $R < 0.5$ and backscatter $R > 0.5$, implying a threshold of $R_0 = 0.5$ for the resolution step-function defined in Equation 2.

2.4. Experimental Setup

After choosing to combine backscatter and isopycnal height diffusion by applying them in complementary regions using a resolution function, we decided on the following four simulations. The control run, REF, uses a Smagorinsky-like biharmonic viscosity and includes no isopycnal height diffusion, isopycnal tracer diffusion, or backscatter. This setup is similar to the reference simulation in OM4 (Chang et al., 2023), however, the FESOM2 reference simulation (Juricke, Danilov, Koldunov, Oliver, Sein, et al., 2020) uses an isopycnal tracer diffusivity of

$3000\,\mathrm{m^2 s^{-1}}$ that is locally scaled relative to their 1° grid spacing at the equator. Our second simulation, GM, is identical to REF except that GM uses both isopycnal height diffusion (Gent & McWilliams, 1990) and isopycnal tracer diffusion (Redi, 1982; Solomon, 1971) wherever $R = L_d/\Delta < 0.5$. Both diffusivities share an equivalent barotropic squared vertical structure with a surface value of $1,000\ \mathrm{m^2\ s^{-1}}$. We also apply a cubic tapering to the isopycnal height diffusivity (but not the isopycnal tracer diffusivity), scaling it to zero where the ocean depth is shallower than 250 m.

Setting the isopycnal height and tracer diffusivities equal is a considerable simplification, resulting in a strictly downgradient horizontal tracer flux (Griffies, 1998). However, diagnostics from eddy-resolving simulations show that the effective tracer and height diffusivities can differ in magnitude, vertical structure, and orientation relative to the mean flow (Abernathey et al., 2013).

In addition to the REF and GM simulations, we also run two backscatter simulations: GM + MBK, which uses a modified form of the Jansen et al. (2019) scheme, and GM + LBK, which uses the Leith + E scheme. In both cases, we include isopycnal height diffusion and isopycnal tracer diffusion as in GM, and we apply backscatter wherever $R = L_d/\Delta > 0.5$.

In the GM + MBK simulation, we use the Jansen et al. (2019) scheme, but we disable the co-located isopycnal height diffusivity as in Chang et al. (2023). Following Yankovsky et al. (2024), we prescribe an equivalent barotropic squared vertical structure for the Laplacian anti-viscosity. The subgrid-scale kinetic energy budget then is

$$\partial_t e = \dot{e}_{\nu_4} - \dot{e}_{\nu_2} - \dot{e}_{\mathrm{diss}} + \dot{e}_{\mathrm{trans}}, \tag{3}$$

where $\dot{e}_{\nu_4}$ is the energy source from biharmonic dissipation, $-\dot{e}_{\nu_2}$ is the energy sink due to backscatter represented as a negative Laplacian viscosity, $-\dot{e}_{\mathrm{diss}}$ is the energy sink due to dissipation of subgrid kinetic energy by bottom drag, and $\dot{e}_{\mathrm{trans}}$ is the horizontal transport of subgrid-scale kinetic energy e. The dissipation term is given by

$$\dot{e}_{\mathrm{diss}} = c_d |U_d| \gamma_b^2 e, \tag{4}$$

where $c_d = 0.003$, $U_d^2 = |\mathbf{u}|^2_{z=-D} + \gamma_b^2 U_e^2$, $U_e = \sqrt{2e}$, and $\gamma_b = 2$. The transport term is given by

$$\dot{e}_{\mathrm{trans}} = \nabla \cdot (\kappa_M \nabla e), \tag{5}$$

where

$$\kappa_M = \gamma_\kappa L \sqrt{U_e^2}, \tag{6}$$

and $\gamma_\kappa = 0.75$ following (Grooms, 2017). Here, the length scale L is the minimum of the grid spacing and the effective Rhines scale, $L_\beta = e^{1/4}\beta^{-1/2}$, where β is the effective barotropic potential vorticity gradient (taking into account both planetary vorticity and bottom topography). The Laplacian viscosity is

$$\nu_2 = -cL\sqrt{\max(2e, 0)}\,\phi^2(x, y, z)\, r(R), \tag{7}$$

where $c = 0.075$ and $\phi(x, y, z)$ is the local equivalent barotropic vertical structure. Rather than implementing the exact step-function (2) in the model, we instead approximate it as $r(R) \approx \left[1 + (R/R_0)^{50}\right]^{-1}$ where $R_0 = 0.5$ (Hallberg, 2013).

In the GM + LBK simulation, we apply the Leith + E scheme (Grooms, 2023). Unlike the other three simulations, GM + LBK uses a Leith-like rather than a Smagorinsky-like biharmonic viscosity. The scheme does not use a subgrid-scale kinetic energy budget. Instead, the biharmonic viscosity is calculated with a Leith-type scaling so that the predicted enstrophy dissipation scale lies at the grid scale. The Laplacian anti-viscosity is chosen so that a prescribed fraction c_K of the kinetic energy dissipated by the biharmonic term is returned to the resolved flow. If

the negative-Laplacian and biharmonic viscosity coefficients predicted by the scheme would violate scale-separation bounds ($|\nu_2|$ too large relative to ν_4), the scheme caps the value of ν_2 accordingly.

The resulting expressions are

$$\nu_4 = \left(\overline{\nu_{\mathrm{LE}}^2}\right)^{1/2} \tag{8}$$

for the biharmonic viscosity and

$$\nu_2 = -m^* \nu_4 \tag{9}$$

for the Laplacian viscosity, where

$$\nu_{\mathrm{LE}} = \Upsilon \left(\frac{\Delta}{\pi}\right)^6 \left[\left(\nabla^2 \zeta\right)^2 - m^* \left|\nabla \overline{\zeta}\right|^2\right]^{1/2}. \tag{10}$$

The vertical component of the vorticity is $\zeta = \partial_x u - \partial_y v$ and the biharmonic coefficient is $\Upsilon = 75$. The overline, for example, in $\overline{\zeta}$, denotes a low-pass spatial filter, and m^* is given by

$$m^* = r(R)\,\overline{m} \tag{11}$$

where m is defined by

$$m = \begin{cases} \dfrac{c_K \left|\nabla \zeta\right|^2}{\zeta^2}, & \text{if } c_K \Delta^2 \left|\nabla \zeta\right|^2 < 4\overline{\zeta}^2, \\ \dfrac{4}{\Delta^2}, & \text{otherwise,} \end{cases} \tag{12}$$

and $r(R)$ is the step-function (2), again approximated as $r(R) \approx \left[1 + (R/R_0)^{50}\right]^{-1}$. The low-pass spatial filter is applied here to the lateral velocity and the result is used to compute $\overline{\zeta}$, whereas Grooms (2023) applied the filter directly to the vorticity. The raw biharmonic viscosity ν_{LE} can be very variable at the grid scale, so it is smoothed before use to improve numerical stability. Smoothing tends to reduce large values that are needed to control the enstrophy cascade, so to produce a smooth field that retains large values, the raw coefficient is squared, then smoothed, then the square root is taken.

We set the fraction $c_K = 1$ in Equation 12, so that all energy dissipated by the biharmonic viscosity is returned to the resolved flow. When the amount of backscatter required to re-inject 100% of the energy dissipated by the biharmonic term is too large, Equation 12 reduces the backscatter coefficient to a stable level.

In practice, the Leith biharmonic viscosity is first computed assuming no backscatter (i.e., $m = 0$). Only if this value exceeds the local background hyperviscosity $u_4 \Delta^3$ are ν_2 and ν_4 recomputed with $m \neq 0$; otherwise, ν_4 is set equal to the background and ν_2 is set to zero. Because these two coefficients are diagnosed point-by-point, the amount of backscatter adapts locally to the magnitude of the resolved gradients and the local dissipation rate. Consequently, no vertical structure needs to be prescribed. The condition that backscatter is only active when the Leith biharmonic coefficient rises above the background minimum controls the extent to which backscatter is active in the GM + LBK simulation, especially in the Southern Ocean.

In initial tests using Leith + E backscatter, Agulhas eddies were unrealistically strong. We therefore disabled backscatter (i.e., set $\nu_2 = 0$) whenever the local Rossby number exceeds 0.3, which corrected this issue.

3. Results

This section presents the results of the four 61-year simulations: a reference simulation (REF), a diffusion-only simulation (GM), and two hybrid simulations (GM + MBK and GM + LBK). First, we describe how the

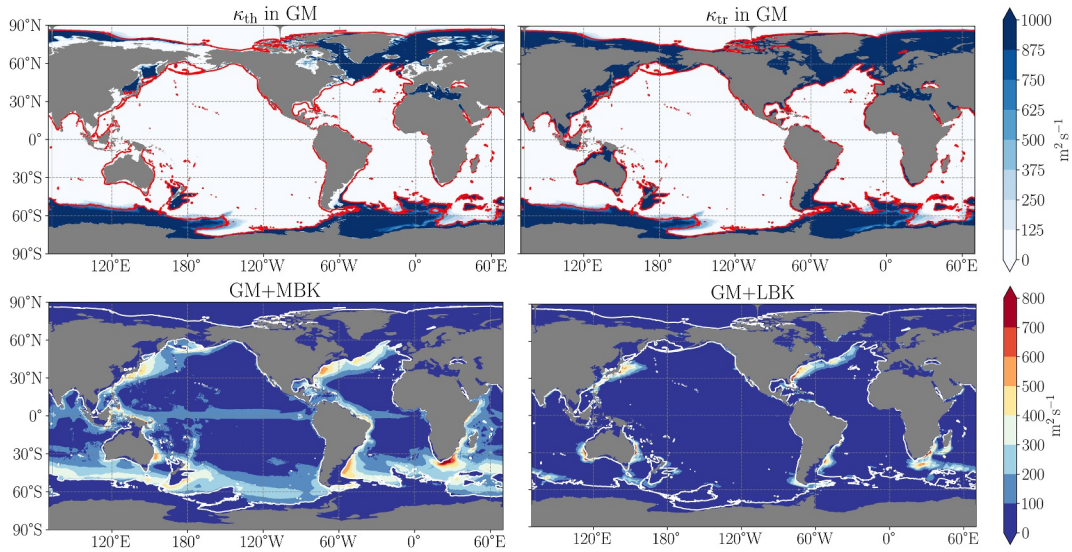

Figure 2. Top: Isopycnal height diffusivity, κ_{th}, and isopycnal tracer diffusivity, κ_{tr}, in the GM simulation, averaged over the final 30 years. These diffusivities are active in regions where $R = L_d/\Delta < 0.5$. Bottom: The negative of the applied Laplacian viscosity (i.e., backscatter anti-viscosity) at the surface in the two backscatter simulations (GM + MBK and GM + LBK), applied only in regions with $R > 0.5$. The red (top)/white (bottom) contour marks $R = 0.5$.

resolution function (2) partitions the ocean in two regions whose boundary evolves in time, and how this evolution is tied to changes in Drake Passage transport. Second, we show that the hybrid schemes increase global kinetic energy by 20%–25% relative to REF, energizing major currents, but avoiding the large, recurring polynyas found in the backscatter-only schemes described in Section 2.2. Third, we demonstrate that the model ocean is sensitive to where backscatter is applied. GM + MBK, which applies backscatter broadly to the Southern Ocean, produces much larger changes in southward heat transport, sea-surface temperature, mixed-layer depth, and Antarctic sea ice than GM + LBK, which instead concentrates it near western boundary currents and applies little in the Southern Ocean. Finally, we show that using a nearly step-like resolution function to apply isopycnal height and tracer diffusion has unexpected consequences. As expected, isopycnal slopes inside the diffusive region are flattened by isopycnal height diffusion, but isopycnal slopes just outside become steeper. The steepening is comparable in magnitude to the flattening produced by backscatter. In Appendix A, we compare the sea surface height in the four simulations with satellite altimetry.

3.1. The Resolution Function

We begin by describing how the resolution function partitions the world ocean into two regions whose boundary evolves in time. In one region, isopycnal height and tracer diffusion are applied ($R < 0.5$), and in the other, backscatter may be applied ($R > 0.5$). Figure 1 shows the time mean distribution of R and the $R = 0.5$ contour. Within the $R > 0.5$ regions, the two hybrid simulations differ in how they apply backscatter: GM + MBK applies it broadly, including over much of the Southern Ocean, whereas GM + LBK confines it mainly to western boundary currents. We then examine how the position of the $R = 0.5$ contour evolves in time and use its variability to infer how backscatter may influence Drake Passage transport.

Figure 1 shows the partitioning into two regions for each simulation, with the black contour marking the $R = L_d/\Delta = 0.5$ isoline. In the model, the resolution function (2) closely approximates a step function (Section 2.4) with a jump located at $R = 0.5$, and the transition between the two regions is negligible. We now describe the $R < 0.5$ and $R > 0.5$ regions in turn.

Where we have less than half a grid cell per deformation radius ($R < 0.5$), we apply a constant value of 1000 m^2 s^{-1} of both isopycnal height and tracer diffusion at the ocean surface. Figure 2 maps these diffusivities in the GM simulation. We taper isopycnal height diffusion to zero over continental shelves shallower than 250 m; isopycnal tracer diffusion, in contrast, remains active there. Consequently, tracer diffusion persists along the eastern US and Brazil continental shelves, whereas height diffusion is almost absent. Both diffusivities cover the

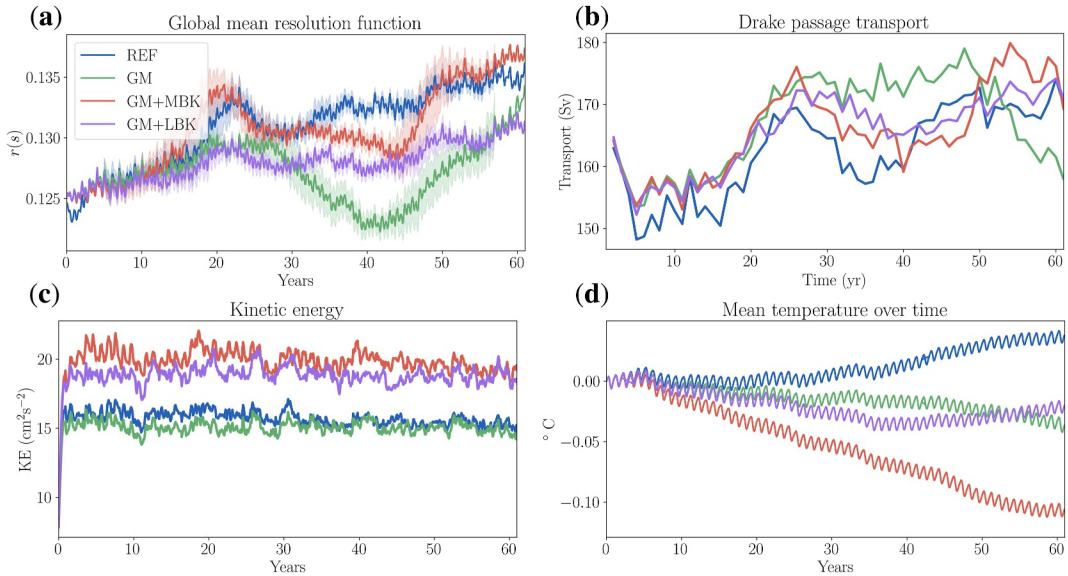

Figure 3. (a) Area averaged resolution function $r(R)$, roughly indicating the fraction of the ocean where isopycnal diffusion is applied, (b) Drake Passage transport, (c) model kinetic energy, (d) mean ocean temperature drift.

North Atlantic Current and large swathes of the Southern Ocean, yet, two Southern Ocean sectors deviate from this pattern. In the South Pacific sector, the $R = 0.5$ contour hugs the Antarctic continent so closely that both diffusivities barely appear. Likewise, between 20°E–60°E (the Indian sector of the Southern Ocean), the contour veers south toward Antarctica, opening another diffusion-free gap. Figure 1 shows that this second gap appears only in the GM and GM + MBK but not in GM + LBK.

Where we have more than half a grid cell per deformation radius ($R > 0.5$), we enable backscatter. Figure 2 shows the negative of the Laplacian viscosity, $-\nu_2$, in the two backscatter simulations, GM + MBK and GM + LBK. Both runs exhibit high $|\nu_2|$ values in western boundary currents; however, GM + MBK (which uses a subgrid-scale kinetic energy budget) produces more expansive fields, with higher values extending farther from major ocean currents. In contrast, in GM + LBK, the negative Laplacian viscosity remains confined to high eddy activity regions. Moreover, in the Southern Ocean, GM + MBK produces a broad continuous band of negative Laplacian viscosity whereas GM + LBK produces only small, isolated patches. Backscatter is only active in the Leith + E scheme when the biharmonic Leith coefficient rises above the background value, which limits the appearance of backscatter at this resolution in the Southern Ocean. Another key difference is the equator, where nonzero values are present in GM + MBK but absent in GM + LBK. This absence in GM + LBK occurs because backscatter is disabled wherever the Rossby number exceeds 0.3.

The resolution function mask boundary at $R = 0.5$ is not static. Because the deformation radius depends on the underlying stratification, the $R = 0.5$ boundary evolves in time (Figure 3a). As a result, the fraction of the ocean where isopycnal height and tracer diffusion are applied fluctuates over time, with the GM simulation showing the most variability of the four simulations and GM + LBK the least. This time dependence explains why each simulation's mean resolution function differs in Figure 1. Moreover, the variability is not uniform along the $R = 0.5$ contour. In Figure 4, we see that the contour is most variable in the Arctic Ocean, along the North Atlantic Current, and in the Southern Ocean. Along the North Atlantic Current, variability is highest in REF relative to the other three simulations, implying that diffusion pins down the boundary's position in the other runs. In contrast, in the Southern Ocean, both REF and GM exhibit substantial variability in the position of the $R = 0.5$ contour; turning on backscatter in GM + MBK and GM + LBK reduces the variability relative to both REF and GM. Relative to REF, GM + MBK retains some variability south of the Agulhas region, whereas it is greatly reduced in GM + LBK. Thus, of the four simulations, GM + LBK has the least variable resolution function boundary.

The time evolution of the resolution function and the Drake Passage transport, shown in Figure 3b, provide a natural experiment for testing how backscatter alters the Drake Passage transport. As the resolution function mask

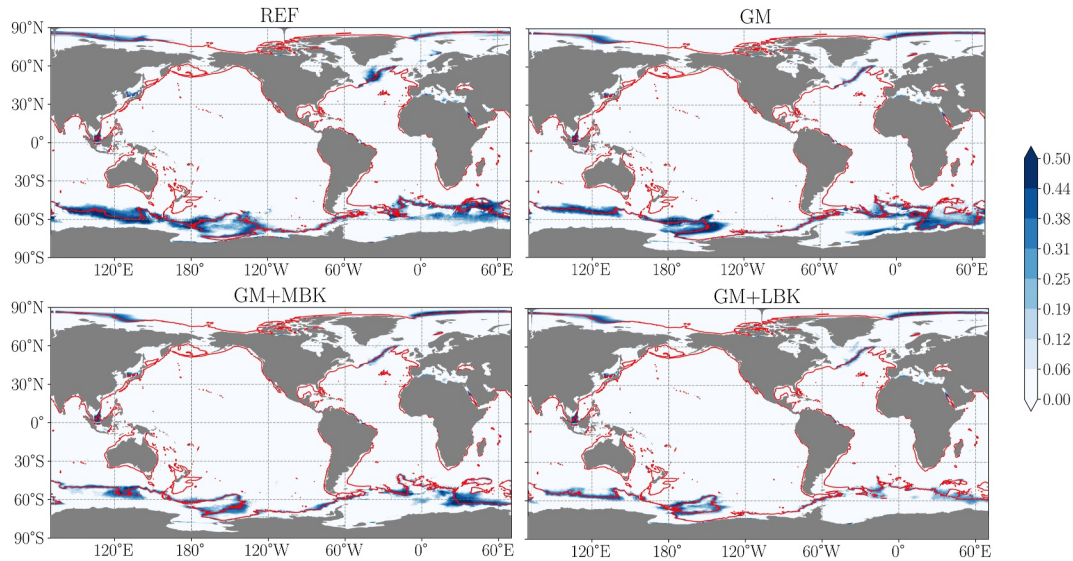

Figure 4. Standard deviation of the resolution function over the final 30 years of each simulation, with darker regions indicating higher temporal variability of the $R = 0.5$ contour. Here, $R = L_d/\Delta$ is the ratio of deformation radius to grid spacing. The red contour marks the threshold $R = 0.5$, separating regions treated with isopycnal height and tracer diffusion from those treated with backscatter.

expands, more of the Southern Ocean is exposed to isopycnal height and tracer diffusion, and a correspondingly smaller area is exposed to backscatter. After removing the multi-decadal drift with a 10-year high-pass filter, the GM simulation shows an instantaneous anti-correlation between Drake Passage transport and resolution function area ($r \approx -0.29$, $p = 0.026$). This finding is expected, as isopycnal height diffusion reduces baroclinic shear, decreasing transport. In GM + MBK, adding backscatter removes the zero-lag anti-correlation and produces a positive lagged response consisting of a cross-correlation peak of +0.36 when the resolution function area leads by 2 years. Granger causality tests (Granger, 1969) on the 10-year high-pass series confirm that the resolution function area contains significant information about future Drake Passage transport, returning p-values of 0.018 at 1 year, 0.047 at 4 yr, and 0.025 at 5 yr lags. Together, these indicate that in GM + MBK, backscatter may be increasing Drake Passage transport. In GM + LBK the zero-lag anti-correlation also disappears, yet no significant lagged correlation emerges, so nothing coherent replaces the GM response.

3.2. How the Hybrid Schemes Energize the Model

Here we examine how diffusion and backscatter modify the model's total kinetic energy, its spatial patterns, and its vertical structure. We begin by considering the volume-integrated kinetic energy. Unlike in adiabatic idealized models where backscatter can increase the kinetic energy by more than an order of magnitude, the kinetic energy here only increases modestly because heat transport constrains how much backscatter we can apply. Then, examining surface kinetic energy, we show that applying isopycnal height and tracer diffusion through a resolution function not only locally damps the flow but also redistributes energy and shifts the paths of ocean currents. We also find distinct responses to backscatter in GM + MBK and GM + LBK. In GM + MBK, backscatter is more effective at energizing the eddy component of the flow in the Southern Ocean, whereas GM + LBK is more effective at energizing the eddy component near western boundary currents. Finally, considering the vertical structure of the flow, we find that backscatter tends to make the flow more barotropic, but the barotropization is displaced from the most strongly energized regions.

We begin by evaluating the volume-integrated kinetic energy across the four simulation. By comparing the GM simulation to the REF simulation, we find that isopycnal height diffusion lowers the model's kinetic energy, averaged over the last 30 years, by about 3%. In contrast, adding backscatter increases the kinetic energy by 27% in GM + MBK and 21% in GM + LBK, relative to REF (Figure 3c). A simple scaling argument shows how modest these gains are.

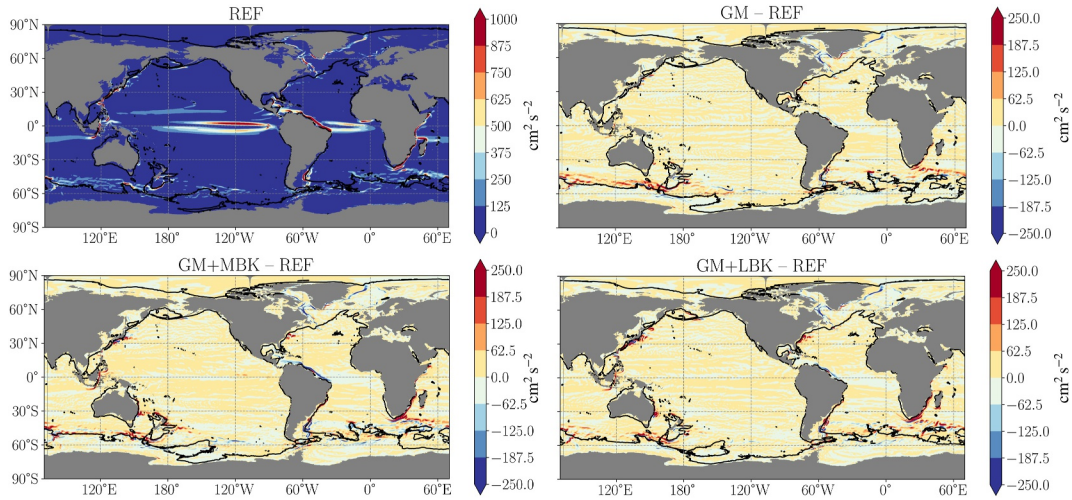

Figure 5. Time-mean surface kinetic energy averaged over the final 30 years of each simulation. The black contour marks the threshold $R = 0.5$, where $R = L_d/\Delta$ is the ratio of deformation radius to grid spacing, which separates regions treated with isopycnal height and tracer diffusion from those treated with backscatter.

In the adiabatic, idealized NeverWorld 2 configuration, refining the grid spacing from 1/4° to 1/32° raises kinetic energy by 500% (Marques et al., 2022). A similar increase appears in the forced NCAR-POP ocean–sea ice model as the grid spacing is refined from 1° to 1/10° (Chassignet et al., 2020). Assuming for simplicity a linear scaling between grid spacing and kinetic energy (the scaling is found to be sublinear in Marques et al. (2022)), a 25% increase in kinetic energy corresponds to an "effective" grid spacing of 1/5°. In principle, we might be able to increase the backscatter coefficient until the model achieves a 500% kinetic energy gain, just as Yankovsky et al. (2024) do in the adiabatic NeverWorld2, matching the coarsened kinetic energy of a model with a 1/32° grid. In practice, however, stronger backscatter increases the poleward heat transport in the Southern Hemisphere, which results in excessive warming of the Southern Ocean and, in the absence of a sufficiently strong isopycnal height diffusivity, unrealistic open-ocean polynyas. The current configurations represent a balance between the desire to energize the model using backscatter against the need to rein in heat transport to plausible levels. This requirement is absent in adiabatic idealized models that have no net meridional heat transport.

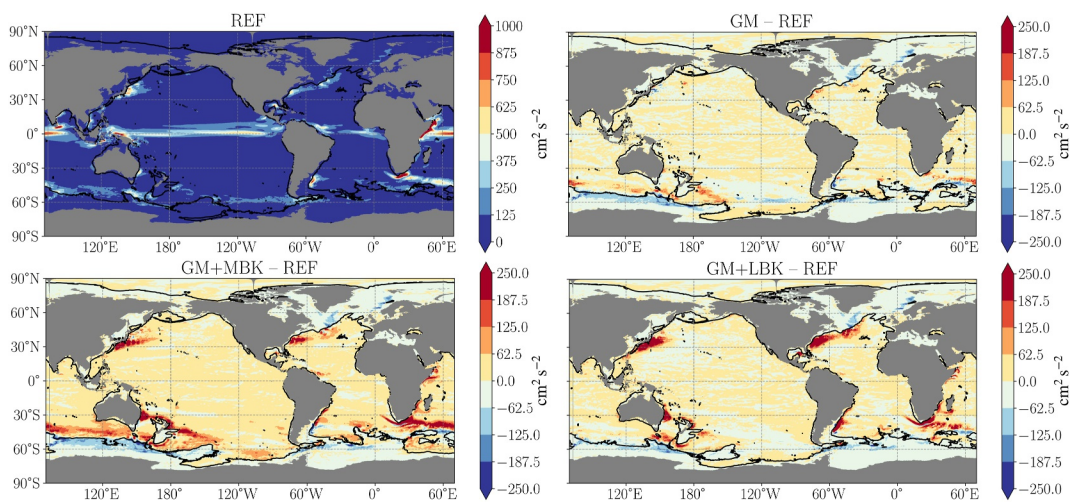

Figure 6. Time-mean eddy kinetic energy averaged over the final 30 years of each simulation. The black contour marks the threshold $R = 0.5$, where $R = L_d/\Delta$ is the ratio of deformation radius to grid spacing, which separates regions treated with isopycnal height and tracer diffusion from those treated with backscatter.

To understand where the changes in kinetic energy occur, we now examine plots of the mean and eddy surface kinetic energy (Figures 5 and 6). We first focus on how applying diffusion modifies the GM simulation in comparison to REF. Beginning with mean surface kinetic energy (Figure 5), we see that some significant mean flows fall in the $R < 0.5$ region in REF. These include mean currents in the Labrador Sea, the Greenland Sea, and parts of the Antarctic Circumpolar Current. Except for the strengthening of a boundary current at the southern tip of Greenland, these currents are greatly weakened with the application of isopycnal height and tracer diffusion in the GM simulation. Surprisingly, however, we also see changes to currents in GM relative to REF in some $R > 0.5$ regions. Whereas some slight weakening occurs in the Pacific, considerable strengthening occurs in a continuous band in the Indian Ocean from Cape Agulhas to the South Australia Basin. The resulting weakening of the currents to the south and strengthening to the north shifts the Antarctic Circumpolar Current equatorwards in the Indian Ocean. Moving on to eddy kinetic energy (Figure 6), we find that eddy kinetic energy within the diffusion region ($R < 0.5$) is greatly reduced in GM relative to REF—especially in the North Atlantic Current and the Southern Ocean. In the Indian sector of the Southern Ocean however, we also see increased eddy activity just north of the $R = 0.5$ contour, so both the mean and eddy components shift northwards there. Eddy activity also increases on the diffusion-free side of the $R = 0.5$ contour near the Gulf Stream and east of New Zealand even though there is little change in the mean flow there. Together, these results show that when isopycnal height and tracer diffusion are applied through a resolution function, they do not simply damp the flow but also redistribute energy and shift the paths of major currents.

We now examine how turning on backscatter in the $R > 0.5$ region modifies these patterns. Three responses emerge. First, relative to both REF and GM, backscatter generally strengthens both the mean and eddy components of western boundary currents, with the energization of the eddy component greatly exceeding that of the mean. Second, the near-continuous band of energized mean flow in the Indian sector of the Southern Ocean weakens in both GM + MBK and GM + LBK when compared to GM. However, the eddy component of this band has distinct responses in the two backscatter simulations. Whereas in GM + MBK the eddy component is greatly energized with the band now extending to the south Pacific, this band is mostly weakened in GM + LBK, with the exception of just west of Cape Agulhas and just south of New Zealand. Taken together, the previous two responses show that GM + MBK is more effective at energizing the eddy component in the Southern Ocean, whereas the GM + LBK is more effective at energizing the eddy component of western boundary currents. Third, relative to both REF and GM, there is a conspicuous weakening in the mean flow of the North Brazil Current, with this weakening extending to the Caribbean Sea. This effect is present in both backscatter simulations, but it is more intense in GM + MBK. Although the mean component weakens, the eddy component either slightly strengthens (in GM + MBK) or remains unchanged (in GM + LBK).

The above discussion focuses on surface currents, but diffusion and backscatter can also alter the vertical structure of the flow. In coarse resolution models, we expect the flow to be more baroclinic because the inverse cascade is not well resolved (Yankovsky et al., 2022). In adiabatic NeverWorld2 simulations, Yankovsky et al. (2024) show that applying backscatter can ameliorate this problem by producing flows as barotropic as a high-resolution reference and almost twice as barotropic at a broad range of latitudes. Inspecting global plots of the barotropic kinetic energy fraction (Figure 7), we see there is a latitude band just south of 30°S where the flow becomes more barotropic relative to REF. This band, however, does not correspond to the band of enhanced kinetic energy but instead lies just north of it. In this enhanced kinetic energy band, the flow instead becomes slightly more baroclinic relative to REF. A similar relationship is found near western boundary currents in both the GM + MBK and the GM + LBK simulations. There, the flow again becomes more barotropic (relative to REF) not where the kinetic energy is enhanced, but in a region just outside it. However, unlike the Southern Ocean, the energized region does not become more baroclinic here.

3.3. Diabatic Consequences of Backscatter

Backscatter not only energizes the model but also produces substantial diabatic effects, especially when it is applied to the Southern Ocean. In GM + MBK, where backscatter energizes Southern Ocean eddies, the ocean cools rapidly over time, southward heat transport increases in the Southern Hemisphere, and the mid-depth residual overturning cell weakens. The increased southward heat transport in the Southern Hemisphere is expressed in the Southern Ocean through the warming of sea surface temperatures, reduced Antarctic sea ice extent, and a southward shift of deep wintertime mixed layers. In contrast, GM + LBK, which applies little backscatter in the

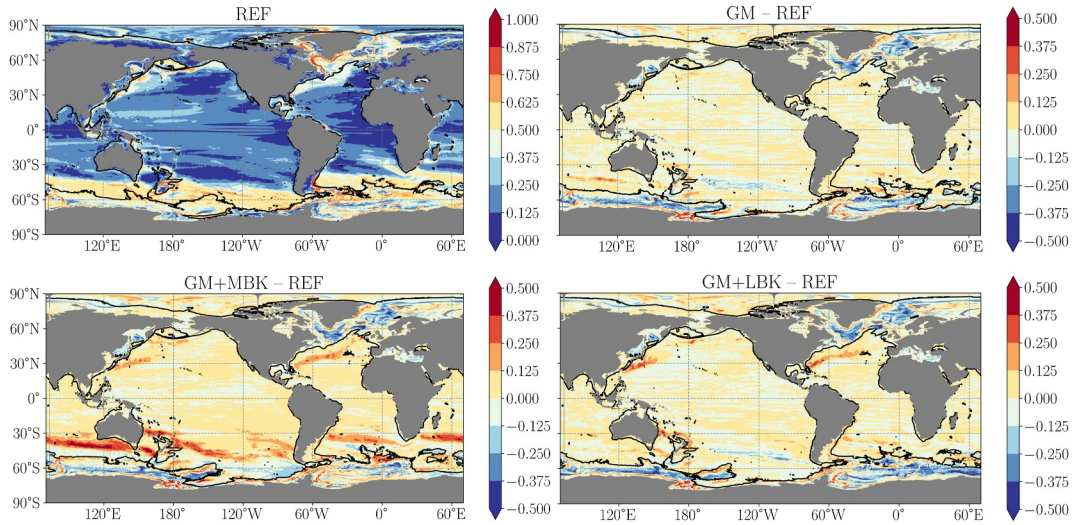

Figure 7. Barotropic kinetic energy fraction computed over the final 30 years of each simulation. The black contour marks the threshold $R = 0.5$, where $R = L_d/\Delta$ is the ratio of deformation radius to grid spacing, which separates regions treated with isopycnal height and tracer diffusion from those treated with backscatter.

Southern Ocean, produces much weaker changes, showing that the diabatic impact of backscatter depends mainly on where backscatter is applied.

To understand the contrasting diabatic responses, we begin by examining how backscatter affects globally averaged temperature. Despite the modest increase in kinetic energy, backscatter enables marginally resolved eddies to perform one of their key roles, which is cooling the ocean through vertical heat transport (Griffies et al., 2015). However, this cooling appears only in GM + MBK, likely because GM + LBK applies far less backscatter in the Southern Ocean. Figure 3d shows that, relative to the initial mean temperature, REF warms over time whereas both GM and GM + LBK cool due to isopycnal height and tracer diffusion. In contrast, the GM + MBK simulation, where backscatter energizes a broad swath of the Southern Ocean, cools rapidly in comparison due to the additional effects of backscatter.

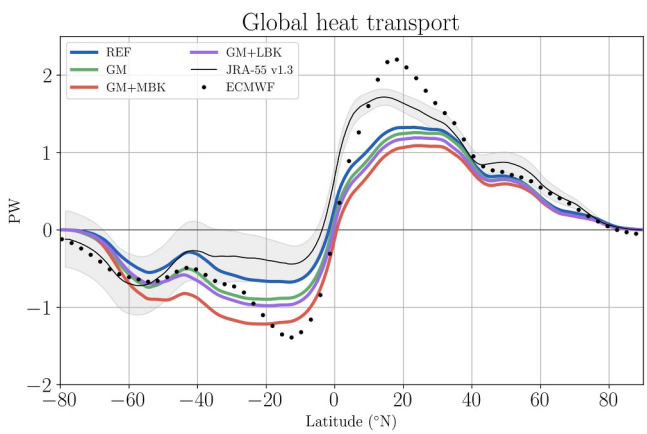

Figure 8. Meridional heat transport averaged over the final 30 years of each simulation. Also shown are estimates derived from two atmospheric reanalysis products: JRA-55 v1.3 (Japan Meteorological Agency, 2013), which shows the mean and range of transport over one annual cycle, and ECMWF (European Centre for Medium-Range Weather Forecasts, 2019) which only shows the mean. Both reanalyzes provide ocean heat transport estimates inferred from atmospheric data.

This enhanced cooling is associated with changes in the meridional heat transport. We quantify these changes in the globally integrated meridional heat transport plot shown in Figure 8. Turning on isopycnal height and tracer diffusion increases southward heat transport, especially in the Southern Hemisphere. When we apply backscatter, the southward heat transport is increased even further in GM + MBK but only slightly in GM + LBK. The reason for this difference likely lies in where backscatter energizes the flow in each simulation. In GM + LBK, backscatter is more effective at energizing western boundary currents, whereas in GM + MBK, backscatter floods the Southern Ocean with eddies. It is these Southern Ocean eddies that induce the increased heat transport. In all cases, the increase in heat transport manifests as a weakening of the mid-depth residual global overturning cell (Figure 9). This change is accompanied by a strengthening of the lower cell and a weakening of the upper cell of the Atlantic Meridional Overturning Circulation. These findings are consistent with backscatter in FESOM2 (Juricke, Danilov, Koldunov, Oliver, & Sidorenko, 2020, see their Figure 10), and mirror the expected effects of isopycnal height diffusion on the overturning cell in low-resolution models (Marshall et al., 2017, see their Figures 3, 4 and 6). However, unlike the backscatter implementation in OM4, we do not find a local strengthening of the upper Atlantic overturning cell between 20°N–40°N (Chang et al., 2023, see their Figure 2).

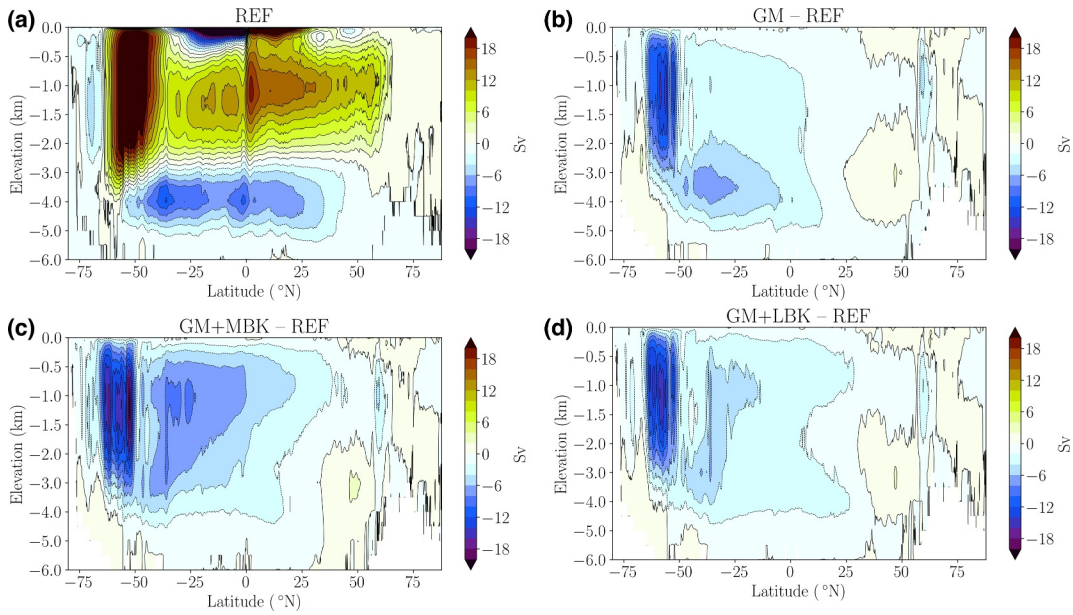

Figure 9. Residual global overturning circulation averaged over the final 30 years of each simulation. (a) Reference simulation (REF). (b–d) Differences relative to REF: (b) GM–REF, (c) GM + MBK–REF, (d) GM + LBK–REF.

The increase in Southern Hemisphere southward heat transport is expressed in three main ways. First, it raises sea surface temperatures in the Southern Ocean (relative to REF), particularly in the South Pacific (Figure 10). In the REF simulation, aside from a few cold patches, the Southern Ocean is already warmer than observations. In GM, there is slight cooling in the Indian sector and slight warming in the Atlantic sector, but the most visible change is the warming centered in the South Pacific. In GM + MBK, cooling in the Indian sector diminishes but a localized cooling appears just south of Cape Agulhas. The most striking change, however, is the intensification and southeastward shift of the South Pacific warming. In contrast, the GM + LBK simulation displays less intense South Pacific warming than even the GM simulation. Thus, a robust response to backscatter in global ocean–sea

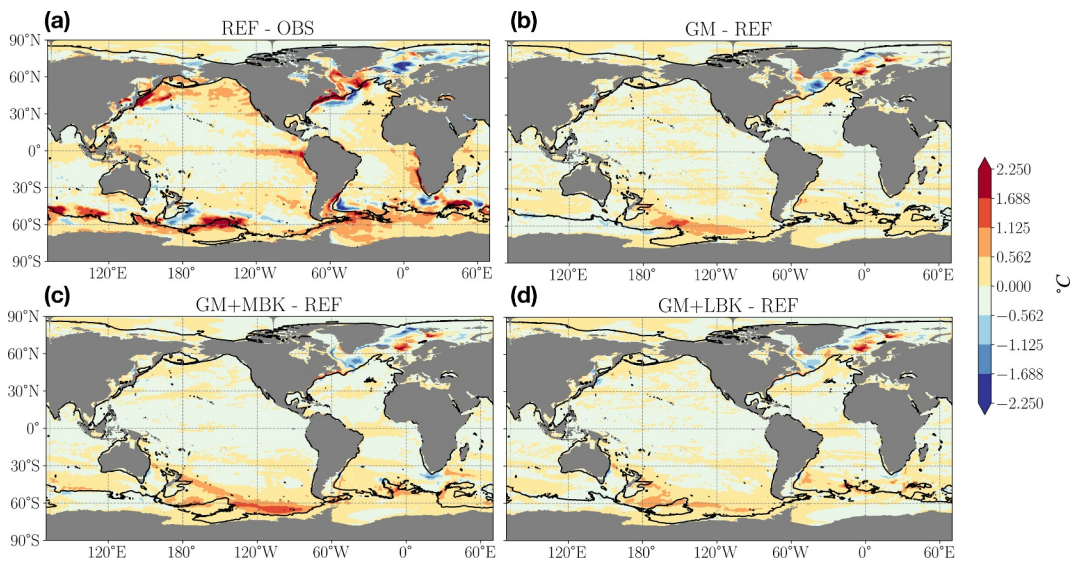

Figure 10. Time-mean sea surface temperature plots averaged over the final 30 years of each simulation. Panel (a) shows the difference between the REF simulations and the observational sea surface temperature climatology from the World Ocean Atlas 2018 (WOA18) (Locarnini et al., 2018). Panels (b–d) show differences relative to REF for GM, GM + MBK, and GM + LBK. The black contour marks the threshold $R = 0.5$, where $R = L_d/\Delta$ is the ratio of deformation radius to grid spacing, which separates regions treated with isopycnal height and tracer diffusion from those treated with backscatter.

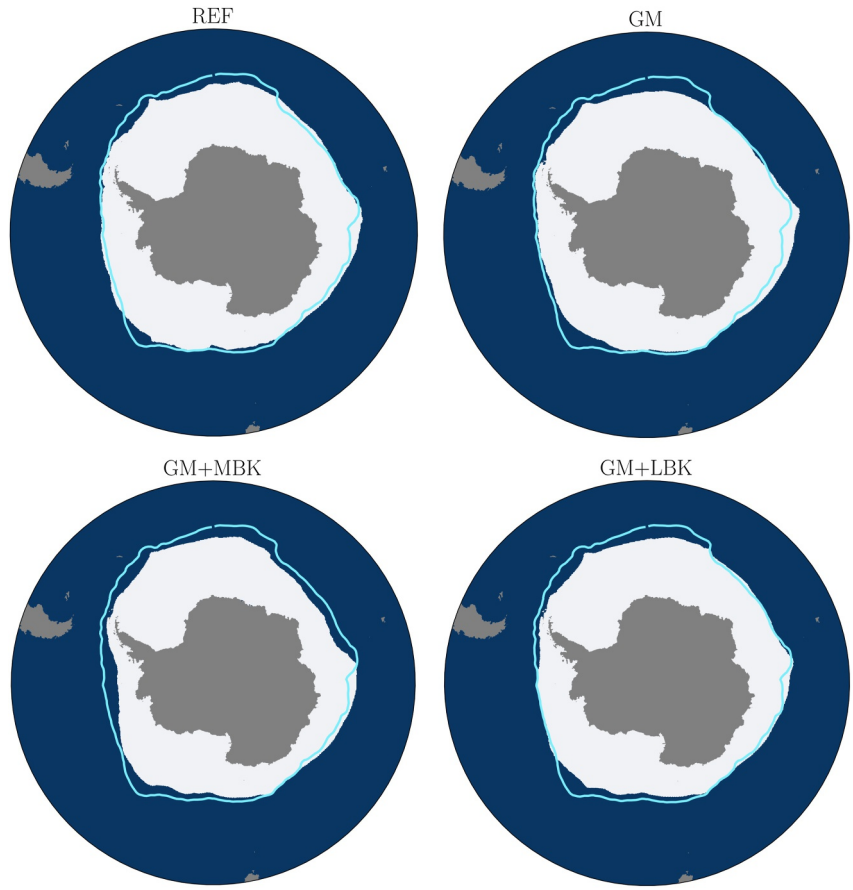

Figure 11. Time-mean sea ice extent (using a threshold of 0.15) from model simulations (REF, GM, GM + MBK, and GM + LBK), averaged over the final 30 years of each simulation. The cyan contour indicates the observed 0.15 concentration threshold, derived from the satellite-based sea ice concentration data set distributed by the National Snow and Ice Data Center (Hurrell et al., 2008; Shea et al., 2020).

ice models is a warming of the Southern Ocean, albeit only when backscatter is applied there (Chang et al., 2023; Juricke, Danilov, Koldunov, Oliver, & Sidorenko, 2020).

In contrast to the Southern Ocean response, GM + MBK and GM + LBK, unlike previous backscatter simulations in FESOM2 and OM4, do not correct the sea surface temperature bias in the North Atlantic. Chang et al. (2023) show that reducing the warm bias along the eastern US coast and the cold bias in the North Atlantic Current require applying backscatter near the Flemish Cap. However, in our runs, the Flemish Cap region is within $R > 0.5$ region where isopycnal height and tracer diffusion (not backscatter) are applied. The model response here is due in part to isopycnal tracer diffusion in the $R > 0.5$ region and due in part to backscatter in the $R < 0.5$ region. In the GM simulation, isopycnal tracer diffusion produces a thin intense warming along the current. With backscatter, in either the GM + MBK or the GM + LBK, some slight cooling occurs outside the resolution function (where $R > 0.5$).

Second, increased southward heat transport results in reduced sea ice extent and thickness in the Southern Hemisphere (Northern Hemisphere sea ice is unchanged). For the first 40 years, GM + MBK has the lowest September sea ice area, followed by GM + LBK, then GM, and finally REF, consistent with the level of heat transport in each simulation (time series not shown). In the last 21 years, however, GM and GM + LBK switch positions so that GM + LBK has the closest sea ice area to REF. Although Figure 11 shows a similar sea ice extent for both GM and GM + LBK, the GM simulation has lower sea ice concentration whereas GM + LBK has concentrations closer to REF (sea ice concentration not shown). GM + MBK has both the smallest sea ice extent and concentration. The reduction in sea ice concentration in GM and GM + MBK occurs in different regions. In GM, sea ice concentration is reduced nearly everywhere, but especially in the Ross Sea. In contrast, in

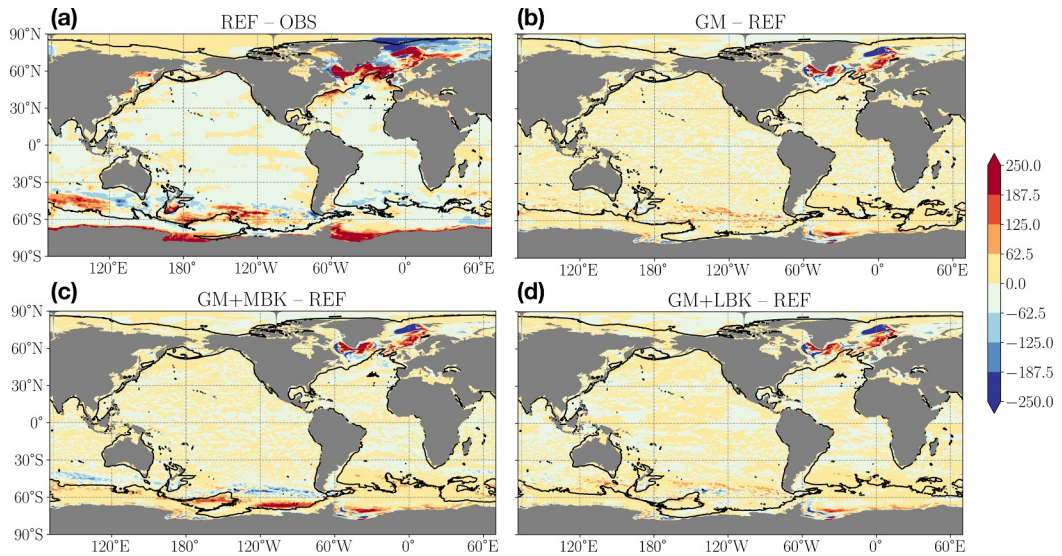

Figure 12. Time-mean winter mixed-layer depth over the final 30 years of each simulation. Panel (a) shows the difference between the REF simulation and the observational mixed layer depth climatology from (de Boyer Montégut et al., 2004), computed using a density threshold criterion of 0.03 kg m^{-3} from the 10 m depth value. Panels (b–d) show differences relative to REF for GM, GM + MBK, and GM + LBK.

GM + MBK, sea ice area is reduced in the South Atlantic and, especially, the Indian Ocean, where sea ice retreats toward the Antarctic coast. A similar decrease in sea ice was also observed in Juricke, Danilov, Koldunov, Oliver, Sein, et al. (2020).

Third, the increased heat transport shifts mixed layers toward the Antarctic coast (Figure 12). In the GM simulation, Southern Ocean mixed layers slightly deepen in the South Pacific relative to REF. Otherwise, changes in mixed-layer depth are mainly restricted to the Labrador Sea and the Greenland Sea. In the GM + MBK simulation, we see a broad dipole in mixed-layer depth across the Indian and Pacific sectors of the Southern Ocean consisting of shallowing in the north and deepening in the south, indicating a southward shift of deeper wintertime mixed layers relative to REF. However, these changes do not consistently improve biases in REF, and the deepening in the southeast Pacific creates a new bias there. In contrast, there is little change in GM + LBK mixed layers beyond those already found in GM.

3.4. Isopycnal Slopes and a Step-Resolution Function

Finally, we assess how isopycnal slopes respond to isopycnal height and tracer diffusion, as well as backscatter, when the diffusion and backscatter are applied in complementary regions using a nearly step-like resolution function. As expected, we find that height diffusion flattens slopes where it is applied. However, applying isopycnal height and tracer diffusion in a nearly discontinuous manner steepens slopes in regions where diffusion is not applied. Backscatter then modulates these patterns in region-dependent ways, flattening isopycnal slopes in some parts of the Southern Ocean while steepening them in others. Although backscatter generally flattens isopycnal slopes, its reduction is smaller on average than the steepening caused by the near-discontinuous application of isopycnal height and tracer diffusion.

Table 1 quantifies the changes in isopycnal slopes for the GM, GM + MBK, and GM + LBK simulations relative to REF. It confirms that isopycnal slopes are flattened in regions where height diffusivity is applied, with a mean slope difference of -7.5×10^{-4} relative to REF (calculated in regions where $R < 0.2$). Surprisingly, however, slopes steepen relative to REF just beyond the areas where diffusion is applied, with a mean change of 1.3×10^{-4} (calculated in regions where $R > 0.8$).

The spatial pattern of flattening and steepening are shown in Figure 13. These patters are evident in the Southern Ocean of the GM simulation where flattening and steepening are apparent on either side of the $R = 0.5$ contour. In the western Pacific sector of the Southern Ocean (140°W–180°W), there is a north-south dipole, with flattening

Table 1
Mean Isopycnal Slope Differences (in Units of 10^{-4}) for the Full-Depth Column

Region	GM	GM + MBK	GM + LBK
Global	+0.0355	−0.3721	−0.8020
$R < 0.2$	−7.5206	−6.1134	−9.5268
$R > 0.8$	+1.2731	+0.7284	+0.7570

Note. Isopycnal height diffusion is applied where $R < 0.5$ and backscatter is applied where $R > 0.5$. For this calculation, we only included regions where all three resolution functions satisfied $R > 0.8$ or $R < 0.2$. Positive values mean that the eddy-parameterized run has steeper slope than REF.

of isopycnal slopes to the south of the $R = 0.5$ contour and steepening to the north. This steepening corresponds to the enhanced surface kinetic energy we found in Figure 6 for the GM simulation. Steeper isopycnal slopes also occur in the eastern Pacific sector close to the Antarctic margin (80°W–140°W) as well as in the Indian Ocean sector. Steepening is likewise found just beyond the resolution function boundary in western boundary currents such as the Gulf Stream and the Brazil Current. In both of these areas, isopycnal height diffusion has been cubically tapered to zero where the depth is less than 250 m, so we mostly have isopycnal tracer diffusion within the $R < 0.5$ region. Consequently, although the flattening within the $R < 0.5$ region is attributable to isopycnal height diffusion, the steepening in the $R > 0.5$ region may be a non-local consequence of isopycnal tracer diffusion applied in a nearly discontinuous manner.

Having described the effects on isopycnal slopes associated with isopycnal height and tracer diffusion, we now turn to backscatter. Relative to REF, backscatter produces flattening in some regions but steepening in others. The Indian sector of the Southern Ocean (and especially the South Australia Basin) displays the clearest flattening signals. Proceeding east, the southwest Pacific dipole that we found in the GM simulation, consisting of steepening in the north and flattening in the south, reverses in both backscatter simulations. In the southeast Pacific (just west of the Drake Passage), GM + MBK exhibits somewhat less steep slopes in the south, but has steeper slopes extending to lower latitudes compared to GM. In contrast to GM and GM + MBK, GM + LBK displays the shallowest slopes in the southeast Pacific. Proceeding to the Atlantic sector, GM + MBK produces slopes steeper than GM, with the steepening again extending to lower latitudes. In contrast, the response of GM + LBK is similar to GM. Both backscatter simulations also show increased steepness along the Antarctic continental slope. Outside the Southern Ocean, the two backscatter simulations further steepen isopycnal slopes around the Gulf Stream and the Brazil Current. Integrated over the region $R > 0.8$, the non-local steepening effect, due to applying isopycnal height and tracer diffusion in a nearly discontinuous manner, exceeds the flattening effects of backscatter (Table 1). Nevertheless, when averaged globally, both GM + MBK and GM + LBK produce slopes less steep than REF.

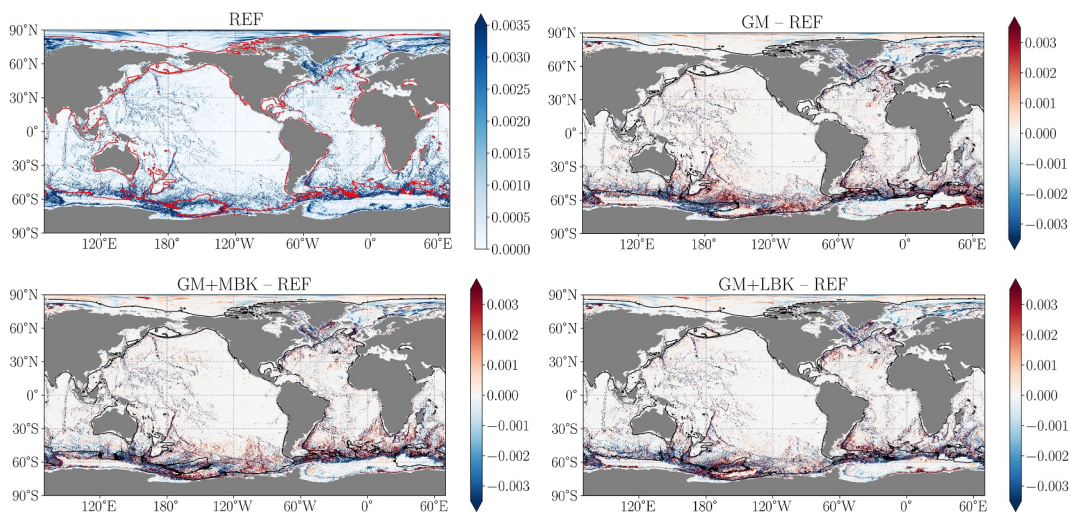

Figure 13. Maps of the basin-wide, depth-averaged, isopycnal slope calculated from time-mean density fields over the final 30 years of each simulation. The top left panel shows the absolute mean slope in the REF simulation. The remaining panels show the difference from REF. The red contour marks the threshold $R = 0.5$, where $R = L_d/\Delta$ is the ratio of deformation radius to grid spacing, which separates regions treated with isopycnal height and tracer diffusion from those treated with backscatter.

4. Discussion

4.1. Backscatter Eddies

Ocean mesoscale eddies flatten isopycnal slopes, controlling the ocean's mean stratification; transporting heat horizontally, moderating meridional temperature gradients; and transporting heat vertically, influencing ocean heat uptake. Here, we examine the extent to which backscatter helps the marginally resolved eddies in a 1/4° model perform these three roles.

In contrast to isopycnal height diffusion, which directly flattens isopycnal slopes, backscatter energizes small-scale eddies, enabling them to cascade to larger scales and convert available potential energy to kinetic energy. In idealized, adiabatic models, this strategy works well. Yankovsky et al. (2024) used backscatter to match both the kinetic and available potential energy of a low-resolution simulation to a high-resolution reference, showing considerable improvements in the mean position of isopycnal surfaces. However, in our diabatic, global simulations, we found that backscatter's ability to flatten isopycnal slopes was modest. Backscatter flattened isopycnal slopes in some regions (e.g., Indian sector of the Southern Ocean), but steepened them in others (e.g., western boundary currents). This weaker flattening signal likely reflects the smaller backscatter amplitude in our simulations compared to Yankovsky et al. (2024). Because stronger backscatter amplitudes would have driven an unrealistically large Southern Hemisphere heat transport, we limited the backscatter amplitude to a level that raised kinetic energy by only 20%–25%, far below the approximately 500% increase in Yankovsky et al. (2024). Given this lower kinetic energy gain and the fact that the vertical structure of our Laplacian anti-viscosity was tuned by Yankovsky et al. (2024) to produce the correct available potential energy after a 500% kinetic energy gain, the weak flattening is unsurprising. If heat transport constraints limit how much kinetic energy can be added through backscatter in global models, then adopting a less surface-intensified vertical structure (or even returning to a depth-independent vertical structure as in Jansen et al. (2019)) could improve isopycnal flattening by backscatter.

The same constraint on backscatter magnitude also explains why the strong barotropization of the flow reported by Yankovsky et al. (2024) appears much weaker here. In their adiabatic setup, the backscatter magnitude could be made large enough to nearly double the barotropic kinetic energy fraction across a wide range of latitudes, matching that of a high-resolution reference. However, in our global simulations, where heat-transport constraints cap backscattere magnitude, the increase in barotropization is much smaller and restricted to western boundary currents and parts of the Southern Ocean. Increasing the barotropic energy fraction would likely requires substantially larger backscatter amplitudes, but these will produce an unrealistically large Southern Hemisphere heat transport.

Although backscatter's ability to flatten isopycnal slopes and barotropize the flow is limited in our simulations, its ability to increase heat transport is strong, especially when applied to the Southern Ocean. Previous backscatter simulations with FESOM2 and OM4 (Chang et al., 2023; Juricke, Danilov, Koldunov, Oliver, & Sidorenko, 2020) both produced a warming of Southern Ocean sea surface temperatures and Juricke, Danilov, Koldunov, Oliver, and Sidorenko (2020) also reported an unrealistic reduction in sea ice. Similarly, our initial tests (Section 2.2) show unrealistically large heat transports and recurring Weddell Sea polynyas. Even after eliminating the polynyas by applying isopycnal height diffusion to parts of the Southern Ocean, we had to limit our backscatter amplitude in the GM + MBK simulation to avoid excessive heat transport. However, Southern Ocean warming depends on where backscatter is applied. We saw strong warming in the GM + MBK simulation, which applied backscatter broadly over large parts of the Southern Ocean. Conversely, our GM + LBK simulation, which applied backscatter to small, isolated regions, showed little increase in heat transport and even showed a cooling relative to the GM simulation.

Backscatter therefore consistently increases horizontal heat transport and warms Southern Ocean sea surface temperatures when applied there. Whether this warming reduces model biases in the Southern Ocean depends on the reference simulation used. Compared to our current model and the OM4 configuration in Chang et al. (2023), the FESOM2 model in Juricke, Danilov, Koldunov, Oliver, and Sidorenko (2020) had the coolest Southern Ocean sea surface temperatures, generally below observations. Therefore, the backscatter-induced warming of the Southern Ocean reduced sea surface temperature biases there. The OM4 reference exhibits a warm sea surface temperature bias in the Southern Ocean, so backscatter-induced warming exacerbates them. The Southern Ocean

in our REF simulation is even warmer than in OM4, and unsurprisingly, its heat balance is particularly sensitive to backscatter.

That the bias reduction depends on the reference simulation might suggest that the issue may lie not with backscatter but with an overly warm reference. If so, then refining a 1/4° grid should consistently warm the Southern Ocean, however, it is not clear that such a warming generally occurs. In the ACCESS-OM2 ocean–sea ice model (Kiss et al., 2020), the 1/4° model has warm biases in the South Atlantic and cool biases in the South Pacific. The 1/10° model cools the South Atlantic, eliminating the warm bias there, but leaves the South Pacific cool biases in place. Similarly, Iovino et al. (2023) compares two forced ocean–sea ice NEMO configurations: the 1/4° ORCA025 with the 1/16° GLOB16. Whereas ORCA025 generally has warm sea surface temperature biases across most of the Southern Ocean, GLOB16 either eliminates these biases in the South Atlantic and South Pacific or replaces them with cold biases. In both of these cases, the grid refinement is accompanied by changes in the lateral parameterizations, so the temperature changes cannot be ascribed to grid refinements alone. Thus, while backscatter consistently warms the Southern Ocean when it is applied there, it is not clear whether refining the grad spacing does so as well.

Backscatter eddies also cool the ocean through vertical heat transport, as expected (Griffies et al., 2015). However, as with horizontal heat transport, this effect only appears when backscatter is applied broadly over the Southern Ocean. This finding again emphasizes the model's sensitivity to the spatial distribution of backscatter, especially over the Southern Ocean.

4.2. Resolution Function Thresholds for Diffusion and Backscatter

In our simulations, we used a sharp resolution function that partitioned the ocean into two regions: one where isopycnal height and tracer diffusion are applied and one where backscatter may be applied. The boundary between the two regions evolves in time with the mean ocean state. Although we were compelled to use isopycnal height diffusion because of its ability to arrest polynya formation, we argued in Section 2.3 why such an approach is desirable. Namely, there is a lower bound below which we expect backscatter to no longer be effective, and in those regions, some form of eddy parameterization is necessary. From idealized simulations (Grooms, 2023; Hallberg, 2013; Jansen & Held, 2014; Jansen et al., 2015), we determined that this bound is approximately $R = L_d/\Delta = 0.4$–0.5. However, whether the threshold remains close to these values in a realistic global model is an open question. There are indications that, in such realistic models, this bound might be lower. For one, backscatter is highly effective at energizing the Southern Ocean despite it being close to the $R = 0.5$ threshold. A second indication is that it is necessary to apply backscatter near the Flemish Cap, which lies in the $R < 0.5$ region, to reduce the North Atlantic sea surface temperature bias (Chang et al., 2023). In highly idealized quasigeostrophic models, values of R smaller than 0.5 correspond to nearly laminar flows with weak velocity gradients, weak dissipation, and hence weak backscatter. In realistic global models, by contrast, additional processes such as wind forcing and topography steering generate velocity gradients, providing more dissipation and therefore more energy for backscatter to return, even where $R < 0.5$. These considerations suggest that we should have used a threshold lower than $R = 0.5$ as the boundary between backscatter and diffusion. They also suggest that further work is required to determine the threshold below which backscatter loses its efficacy in realistic global models.

On the other hand, there are indications that we should have instead used a threshold larger than $R = 0.5$. Hallberg (2013) recommends applying isopycnal height diffusion whenever $R < 2$. This recommendation is based on reproducing eddy-driven transports on both sides of the resolution function: on one side, isopycnal height diffusion parameterizes the transport whereas on the other the grid spacing is fine enough to explicitly resolve them. We chose the $R = 0.5$ threshold partly to limit the application of the diffusivities to the smallest possible area and in the hope that backscatter will energize the marginally resolved eddies outside the resolution function, increasing the resolved transport. However, it is not clear whether this approach succeeded. As we saw above, backscatter's ability to flatten isopycnal slopes was limited, but this may be a consequence of the low backscatter amplitude we used. However, we also found unexpected steepening of isopycnal slopes in the region outside the resolution function. We attributed this steepening to be a non-local consequence of applying isopycnal tracer diffusion in a nearly discontinuous manner because we saw this effect in areas, such as the Gulf Stream, where isopycnal tracer diffusion (but not height diffusion) was mostly applied. However, it is plausible that isopycnal height diffusion is responsible.

These results point to areas where further investigation is needed. First, we need to determine the consequences of applying isopycnal tracer diffusivity in a nearly discontinuous manner, as done here. Second, we need to determine the threshold value R_0 such that we resolve the eddy transports on both sides of the resolution function when we apply isopycnal height diffusion at $R < R_0$ and backscatter at $R > R_0$. We expect R_0 to be smaller than the original $R_0 = 2$ recommendation by Hallberg (2013) because backscatter should be able to increase marginally resolved eddy transports. However, this threshold is probably larger than the $R_0 = 0.5$ used here.

4.3. Balancing Backscatter and Diffusion

The preceding discussion suggests that there are conflicting constraints on selecting the resolution function threshold R_0. The need to energize ocean eddies motivates a lower threshold, whereas reproducing eddy transports motivates a higher one. This tension is resolved by adopting separate resolution functions for diffusion and backscatter, thereby allowing the appropriate range of R values to differ between the two. This observation suggests that a modified form of the Jansen et al. (2019) scheme may provide a path forward, in which diffusion and backscatter are neither co-located, as in Jansen et al. (2019), or located in complementary regions, as done here, but rather each is applied through a separate resolution function. These two resolution functions will likely overlap in space. In the overlap region, extraction of available potential energy by isopycnal height diffusion will act as an energy source to backscatter as in the original Jansen et al. (2019) scheme. This approach will ensure that the model resolves eddy transports everywhere.

However, this approach suffers from the same deficiency as the original Jansen et al. (2019) approach. Isopycnal height diffusion smooths away baroclinic eddies, reducing eddy variability to unrealistic levels. There are two strategies to overcome this damping problem. One option is the scale-aware splitting procedure proposed by Mak et al. (2023), which applies isopycnal height diffusion only to the large-scale flow, leaving mesoscale eddies undamped. The other is the stochastic GM + E closure of Grooms et al. (2025), which backscatters a prescribed fraction of the available potential energy removed by isopycnal height diffusion as random velocity increments. By using random velocity increments rather than a negative Laplacian viscosity, the stochastic scheme can generate variability even when strong diffusion is present. Either approach could allow the scheme to capture eddy transports while still injecting enough energy to maintain realistic eddy kinetic energy in the model.

4.4. Conclusions and Future Outlook

To summarize, when backscatter was used alone in our 1/4° CESM2–MOM6 configuration, it produced unrealistic southward heat transport and large, recurring Weddell Sea polynyas. When we introduced a resolution function that applies isopycnal height and tracer diffusion where $R = L_d/\Delta < 0.5$ and backscatter elsewhere, it arrested polynya formation. The GM + MBK simulation, which uses the Jansen et al. (2019) scheme, energized and barotropized the Southern Ocean but increased southward heat transport and reduced sea ice. In contrast, the GM + LBK simulation, which uses the Leith + E scheme (Grooms, 2023), mainly intensified eddy activity in western boundary currents with a smaller impact on the Southern Ocean. The contrast arises from where backscatter is applied: the Jansen et al. (2019) scheme spreads anti-viscosity broadly whereas the Leith + E scheme concentrates it near boundary currents and applies little in the Southern Ocean. Unlike idealized adiabatic studies where backscatter can increase kinetic energy by roughly 500% to match the kinetic energy of a high-resolution reference (Yankovsky et al., 2024), our gains were limited to 20%–25%, with the magnitude of the backscatter coefficient in the GM + MBK simulation limited by heat transport constraints. In the GM + LBK simulation, heat transport increased only slightly, suggesting that further increases in the backscatter magnitude may be possible using the Leith + E scheme. In this configuration, we recommend confining backscatter primarily to western boundary currents rather than applying it broadly in the Southern Ocean.

Our results emphasize the need to understand backscatter's effects in diabatic models. Backscatter, which was originally designed and tuned in adiabatic idealized settings, can reproduce the kinetic energy and isopycnal structure of a high-resolution reference in such settings. Yet in realistic global models, such as FESOM2, OM4, and our CESM-MOM6 model, backscatter systematically amplifies meridional heat transport whenever it is applied to the Southern Ocean. The Diabatic Neverworld Ocean (DINO) (Kamm et al., 2025) NEMO configuration offers an idealized setting to isolate these diabatic effects. Based on NeverWorld2 (Marques et al., 2022), DINO adds prognostic temperature and salinity equations along with parameterizations for convection and diapycnal mixing. As a next step, we propose testing whether backscatter can simultaneously

reproduce the kinetic energy, available potential energy, and heat transport of a high-resolution reference—essentially, extending the results of Yankovsky et al. (2024) to a diabatic context. Success would determine the mechanism behind the excess heat transport and guide the implementation of backscatter in realistic global ocean models.

Appendix A: Sea Surface Height

This appendix compares the sea surface height (Figure A1) from the four simulations with satellite altimetry. Compared to the AVISO altimetry product (European Union Copernicus Marine Service Information, 2024), which provides globally gridded SSH fields from optimal interpolation of multiple satellite altimeter missions, the SSH in REF exhibits the usual biases in the Gulf Stream and Kuroshio, as well as a tripole bias in the Southern Ocean along the path of circumpolar current. In GM, changes are concentrated in the Southern Hemisphere, with reduced SSH in the Indian Ocean sector and south of Australia, increased SSH in the South Pacific, and decreased SSH in the South Atlantic. However, these changes do not align perfectly with the original biases, so they alleviate them in some areas while exacerbating them in others. GM + MBK shows a similar pattern, with the changes in the SSH failing to align precisely with the original biases. In contrast, GM + LBK produces the smallest changes in SSH, but these adjustments coincide more closely with and mitigate the original biases.

Although the energization does not uniformly reduce SSH biases across the two hybrid simulations,it does reduce some biases in the standard deviation of SSH (Figure A2). Relative to observations, the REF simulation overestimates SSH variability in the Southern Ocean but otherwise underestimates it over most of the ocean, especially near western boundary currents. In GM, the SSH variability bias in the Indian Ocean sector is reduced, but a new bias emerges in the South Pacific. However, although both backscatter simulations maintain the reduced biases in the Indian sector, neither exhibit the new South Pacific bias. In the Indian sector of the Southern Ocean, north of the resolution function threshold, SSH variability increases in GM + MBK but not in GM + LBK. Both simulations exhibit increased SSH variability near western boundary currents, with a stronger increase in GM + LBK. Moreover, comparing these enhancements near the Gulf Stream and Kuroshio with biases in REF reveals that they are displaced too far south and fail to extend far enough into the basin interior (a similar problem

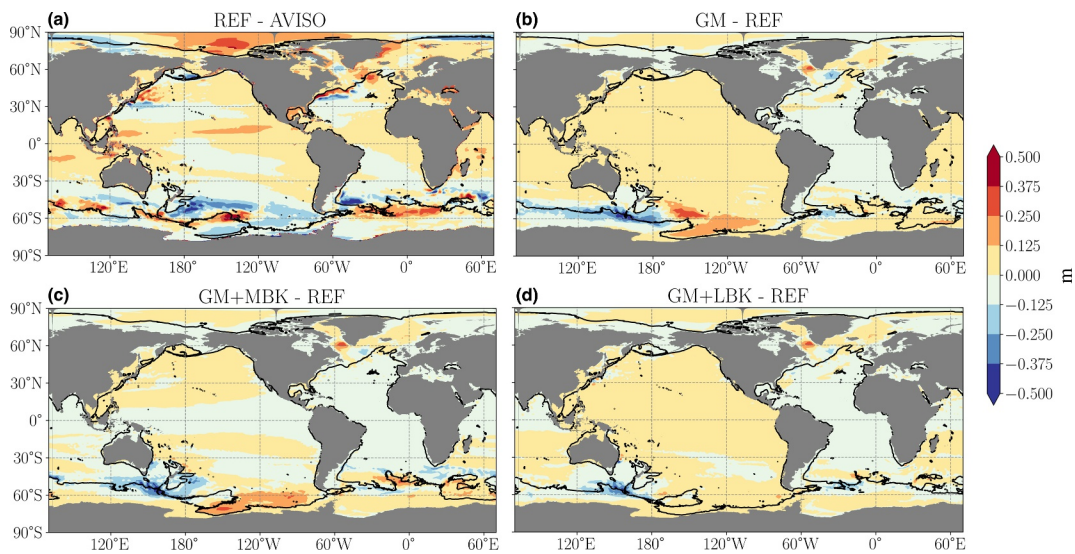

Figure A1. Time-mean sea surface height averaged over the final 30 years of each simulation. Panel (a) shows the difference between the REF simulation and sea surface height fields derived from AVISO (European Union Copernicus Marine Service Information, 2024). Panels (b–d) show differences relative to REF for GM, GM + MBK, and GM + LBK. The black contour marks the threshold $R = 0.5$, where $R = L_d/\Delta$ is the ratio of deformation radius to grid spacing, which separates regions treated with isopycnal height and tracer diffusion from those treated with backscatter.

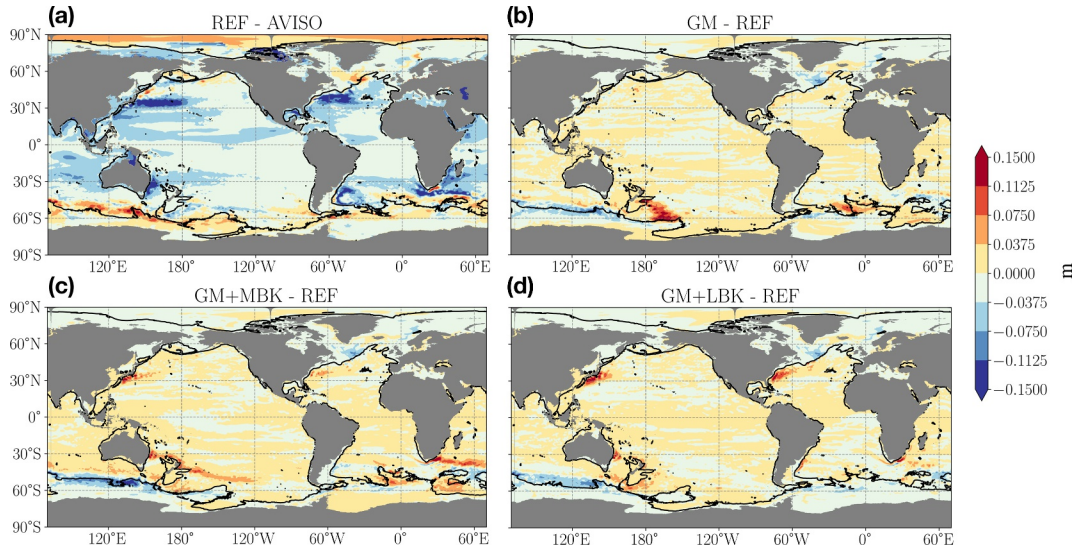

Figure A2. Standard deviation of sea surface height averaged over the final 30 years of each simulation. Panel (a) shows the difference between the REF simulation and sea surface height fields derived from AVISO (European Union Copernicus Marine Service Information, 2024). Panels (b–d) show differences relative to REF for GM, GM + MBK, and GM + LBK. The black contour marks the threshold $R = 0.5$, where $R = L_d/\Delta$ is the ratio of deformation radius to grid spacing, which separates regions treated with isopycnal height and tracer diffusion from those treated with backscatter.

is also seen in Juricke, Danilov, Koldunov, Oliver, and Sidorenko (2020)). Similarly, both GM + MBK and GM + LBK increase variability in the East Australian Current, partially reducing the original bias, but this increase does not extend far enough south, leaving the southern bias uncorrected. In the Brazil Current, although the REF simulation underestimates variability, GM + MBK decreases it whereas GM + LBK increases variability but only in a narrow segment of the current.

Conflict of Interest

The authors declare no conflicts of interest relevant to this study.

Availability Statement

The MOM6 code used in this study is available at https://github.com/houssamyassin/MOM6, with the version used archived on Zenodo as described by Hallberg et al. (2025) (https://doi.org/10.5281/zenodo.17901673). CESM case files and diagnostic notebooks can be found at https://github.com/houssamyassin/MOM6-analysis, with an archived version available on Zenodo as described by Yassin (2025) (https://doi.org/10.5281/zenodo.17901066). Model output is available on the Derecho computer at `/glade/campaign/cesm/development/omwg/projects/MOM6/eddy_cpt/`. Atmospheric reanalysis data were obtained from the ERA5 reanalysis produced by Copernicus Climate Change Service (C3S) (2020) and accessed via the Copernicus Climate Data Store (https://cds.climate.copernicus.eu, https://doi.org/10.24381/cds.adbb2d47), and from the Japanese 55-year Reanalysis (JRA-55) produced by Japan Meteorological Agency (2013) and distributed through the NCAR Research Data Archive (https://rda.ucar.edu/datasets/ds628.1, https://doi.org/10.5065/D6HH6H41). Sea surface height observations are from the AVISO global delayed-time gridded altimeter product distributed by European Union Copernicus Marine Service Information (2024) (https://data.marine.copernicus.eu, https://doi.org/10.48670/moi-00148). Sea surface temperature climatology is based on the World Ocean Atlas 2018 temperature fields of Locarnini et al. (2018) (https://www.ncei.noaa.gov/products/world-ocean-atlas, https://doi.org/10.25921/2c8h-sa89). Mixed layer depth climatology is from de Boyer Montégut et al. (2004), available from IFREMER (https://www.ifremer.fr/cerweb/deboyer/mld, https://doi.org/10.1029/2004GL021592). Sea-ice concentration forcing in this study is based on the merged Hadley–OI sea surface temperature and sea ice concentration data set described by Shea et al. (2020) and Hurrell et al. (2008), available from the UCAR/NCAR DASH Repository (https://doi.org/10.5065/r33v-sv91).

Acknowledgments
The authors thank Gokhan Danabasoglu for suggesting the use of isopycnal height diffusion to arrest polynya growth. We also thank Elizabeth Yankovsky and an anonymous reviewer for helpful suggestions that have improved the clarity of the text. We gratefully acknowledge the members of the Ocean Transport and Eddy Energy Climate Process Team for their insightful discussions throughout the course of this project. HY and IG are supported by NSF Grant 1912332. GM is partially supported by the NSF Grant 1912420. This material is based upon work supported by the National Center for Atmospheric Research (NCAR), which is a major facility sponsored by the NSF under cooperative agreement no. 1852977. Computing resources (https://doi.org/10.5065/qx9a-pg09) were provided by the Climate Simulation Laboratory at NCAR's Computational and Information Systems Laboratory, sponsored by the National Science Foundation and other agencies.

References

Abernathey, R., Ferreira, D., & Klocker, A. (2013). Diagnostics of isopycnal mixing in a circumpolar channel. *Ocean Modelling*, *72*, 1–16. https://doi.org/10.1016/j.ocemod.2013.07.004

Adcroft, A., Anderson, W., Balaji, V., Blanton, C., Bushuk, M., Dufour, C. O., et al. (2019). The GFDL global ocean and sea ice model OM4.0: Model description and simulation features. *Journal of Advances in Modeling Earth Systems*, *11*(10), 3167–3211. https://doi.org/10.1029/2019MS001726

Bachman, S. D. (2019). The GM+E closure: A framework for coupling backscatter with the Gent and McWilliams parameterization. *Ocean Modelling*, *136*, 85–106. https://doi.org/10.1016/j.ocemod.2019.02.006

Bagaeva, E., Danilov, S., Oliver, M., & Juricke, S. (2024). Advancing eddy parameterizations: Dynamic energy backscatter and the role of subgrid energy advection and stochastic forcing. *Journal of Advances in Modeling Earth Systems*, *16*(4), e2023MS003972. https://doi.org/10.1029/2023MS003972

Berner, J., Shutts, G. J., Leutbecher, M., & Palmer, T. N. (2009). A spectral stochastic kinetic energy backscatter scheme and its impact on flow-dependent predictability in the ECMWF ensemble prediction system. *Journal of the Atmospheric Sciences*, *66*(3), 603–626. https://doi.org/10.1175/2008JAS2677.1

Chang, C.-Y., Adcroft, A., Zanna, L., Hallberg, R., & Griffies, S. M. (2023). Remote versus local impacts of energy backscatter on the North Atlantic SST biases in a global Ocean model. *Geophysical Research Letters*, *50*(21), e2023GL105757. https://doi.org/10.1029/2023GL105757

Chassignet, E. P., Yeager, S. G., Fox-Kemper, B., Bozec, A., Castruccio, F., Danabasoglu, G., et al. (2020). Impact of horizontal resolution on global ocean–sea ice model simulations based on the experimental protocols of the Ocean Model Intercomparison Project phase 2 (OMIP-2). *Geoscientific Model Development*, *13*(9), 4595–4637. https://doi.org/10.5194/gmd-13-4595-2020

Copernicus Climate Change Service (C3S). (2020). ERA5: Fifth generation of ECMWF atmospheric reanalyses of the global climate [Dataset]. *Copernicus Climate Change Service*. https://doi.org/10.24381/cds.adbb2d47

Danabasoglu, G., Lamarque, J.-F., Bacmeister, J., Bailey, D. A., DuVivier, A. K., Edwards, J., et al. (2020). The Community Earth System Model Version 2 (CESM2). *Journal of Advances in Modeling Earth Systems*, *12*(2), e2019MS001916. https://doi.org/10.1029/2019MS001916

Danilov, S., Sidorenko, D., Wang, Q., & Jung, T. (2017). The finite-volume sea ice–ocean model (FESOM2). *Geoscientific Model Development*, *10*(2), 765–789. https://doi.org/10.5194/gmd-10-765-2017

de Boyer Montégut, C., Madec, G., Fischer, A. S., Lazar, A., & Iudicone, D. (2004). Mixed layer depth over the global ocean: An examination of profile data and a profile-based climatology. *Journal of Geophysical Research*, *109*(C12), C12003. https://doi.org/10.1029/2004JC002378

European Centre for Medium-Range Weather Forecasts. (2019). ECMWF ORAS5: Ocean Reanalysis System 5 [Dataset]. *Reading, UK: European Centre for Medium-Range Weather Forecasts (ECMWF)*. https://www.ecmwf.int/en/forecasts/dataset/ocean-reanalysis-system-5

European Union Copernicus Marine Service Information. (2024). Global Ocean gridded L4 Sea surface heights and derived variables reprocessed (1993-ongoing) [Dataset]. *Copernicus Marine Environment Monitoring Service (CMEMS)*. https://doi.org/10.48670/moi-00145

Fox-Kemper, B., Danabasoglu, G., Ferrari, R., Griffies, S., Hallberg, R., Holland, M., et al. (2011). Parameterization of mixed layer eddies. III: Implementation and impact in global ocean climate simulations. *Ocean Modelling*, *39*(1–2), 61–78. https://doi.org/10.1016/j.ocemod.2010.09.002

Gent, P. R., & McWilliams, J. C. (1990). Isopycnal mixing in ocean circulation models. *Journal of Physical Oceanography*, 150–155. https://doi.org/10.1175/1520-0485(1990)020⟨0150:imiocm⟩2.0.co;2

Granger, C. W. J. (1969). Investigating causal relations by econometric models and cross-spectral methods. *Econometrica*, *37*(3), 424–438. https://doi.org/10.2307/1912791

Griffies, S. M. (1998). The Gent-McWilliams skew flux. *Journal of Physical Oceanography*, *28*(5), 831–841. https://doi.org/10.1175/1520-0485(1998)028⟨0831:TGMSF⟩2.0.CO;2

Griffies, S. M., Adcroft, A., & Hallberg, R. W. (2020). A primer on the vertical Lagrangian-remap method in ocean models based on finite volume generalized vertical coordinates. *Journal of Advances in Modeling Earth Systems*, *12*(10), e2019MS001954. https://doi.org/10.1029/2019MS001954

Griffies, S. M., & Hallberg, R. W. (2000). Biharmonic friction with a Smagorinsky-like viscosity for use in large-scale eddy-permitting ocean models. *Monthly Weather Review*, *128*(8), 2935–2946. https://doi.org/10.1175/1520-0493(2000)128⟨2935:BFWASL⟩2.0.CO;2

Griffies, S. M., Winton, M., Anderson, W. G., Benson, R., Delworth, T. L., Dufour, C. O., et al. (2015). Impacts on ocean heat from transient mesoscale eddies in a hierarchy of climate models. *Journal of Climate*, *28*(3), 952–977. https://doi.org/10.1175/JCLI-D-14-00353.1

Grooms, I. (2017). Simulations of eddy kinetic energy transport in barotropic turbulence. *Physical Review Fluids*, *2*(11), 113801. https://doi.org/10.1103/physrevfluids.2.113801

Grooms, I. (2023). Backscatter in energetically-constrained Leith parameterizations. *Ocean Modelling*, *186*, 102265. https://doi.org/10.1016/j.ocemod.2023.102265

Grooms, I., Agarwal, N., Marques, G., Pegion, P. J., & Yassin, H. (2025). The stochastic GM + E closure: A framework for coupling stochastic backscatter with the Gent and McWilliams parameterization. *Journal of Advances in Modeling Earth Systems*, *17*(5), e2024MS004560. https://doi.org/10.1029/2024MS004560

Hallberg, R. (2013). Using a resolution function to regulate parameterizations of oceanic mesoscale eddy effects. *Ocean Modelling*, *72*, 92–103. https://doi.org/10.1016/j.ocemod.2013.08.007

Hallberg, R., Adcroft, A., Ward, M., Marques, G., Hedstrom, K., Altuntas, A., et al. (2025). houssamyassin/mom6: V1.0.0 [Software]. *Zenodo*. https://doi.org/10.5281/zenodo.17901673

Hunke, E. C., Lipscomb, W. H., Turner, A. K., Jeffery, N., & Elliott, S. (2015). *CICE: The Los Alamos Sea ice model documentation and software user's manual version 5.0 (Technical Report No. LA-CC-06-012)*. Los Alamos National Laboratory.

Hurrell, J. W., Hack, J. J., Shea, D., Caron, J. M., & Rosinski, J. (2008). A new sea surface temperature and sea ice boundary dataset for the community atmosphere model. *Journal of Climate*, *21*(19), 5145–5153. (Describes development and validation of merged Hadley–OI SST and sea ice concentration data set for CAM boundary forcing). https://doi.org/10.1175/2008JCLI2292.1

Iovino, D., Fogli, P. G., & Masina, S. (2023). Evaluation of the CMCC global eddying ocean model for the Ocean Model Intercomparison Project (OMIP2). *Geoscientific Model Development*, *16*(21), 6127–6159. https://doi.org/10.5194/gmd-16-6127-2023

Jansen, M. F., Adcroft, A., Khani, S., & Kong, H. (2019). Toward an energetically consistent, resolution aware parameterization of ocean mesoscale eddies. *Journal of Advances in Modeling Earth Systems*, *11*(8), 2844–2860. https://doi.org/10.1029/2019MS001750

Jansen, M. F., & Held, I. M. (2014). Parameterizing subgrid-scale eddy effects using energetically consistent backscatter. *Ocean Modelling*, *80*, 36–48. https://doi.org/10.1016/j.ocemod.2014.06.002

Jansen, M. F., Held, I. M., Adcroft, A., & Hallberg, R. (2015). Energy budget-based backscatter in an eddy permitting primitive equation model. *Ocean Modelling*, *94*, 15–26. https://doi.org/10.1016/j.ocemod.2015.07.015

Japan Meteorological Agency. (2013). JRA-55: Japanese 55-year reanalysis, daily 3-hourly and 6-hourly data [Dataset]. *Research Data Archive at the National Center for Atmospheric Research, Computational and Information Systems Laboratory*. https://www.data.jma.go.jp/jra/html/JRA-55/index_en.html

Juricke, S., Danilov, S., Koldunov, N., Oliver, M., Sein, D. V., Sidorenko, D., & Wang, Q. (2020). A kinematic kinetic energy backscatter parametrization: From implementation to Global Ocean simulations. *Journal of Advances in Modeling Earth Systems*, *12*(12), e2020MS002175. https://doi.org/10.1029/2020MS002175

Juricke, S., Danilov, S., Koldunov, N., Oliver, M., & Sidorenko, D. (2020). Ocean kinetic energy backscatter parametrization on unstructured grids: Impact on global eddy-permitting simulations. *Journal of Advances in Modeling Earth Systems*, *12*(1), e2019MS001855. https://doi.org/10.1029/2019MS001855

Juricke, S., Danilov, S., Kutsenko, A., & Oliver, M. (2019). Ocean kinetic energy backscatter parametrizations on unstructured grids: Impact on mesoscale turbulence in a channel. *Ocean Modelling*, *138*, 51–67. https://doi.org/10.1016/j.ocemod.2019.03.009

Kamm, D., Deshayes, J., & Madec, G. (2025). DINO: A diabatic model of pole-to-pole ocean dynamics to assess subgrid parameterizations across horizontal scales. In *EGUsphere* (pp. 1–26). https://doi.org/10.5194/egusphere-2025-1100

Kiss, A. E., Hogg, A. M., Hannah, N., Boeira Dias, F., Brassington, G. B., Chamberlain, M. A., et al. (2020). ACCESS-OM2 v1.0: A global ocean–sea ice model at three resolutions. *Geoscientific Model Development*, *13*(2), 401–442. https://doi.org/10.5194/gmd-13-401-2020

Large, W. G., McWilliams, J. C., & Doney, S. C. (1994). Oceanic vertical mixing: A review and a model with a nonlocal boundary layer parameterization. *Reviews of Geophysics*, *32*(4), 363–403. https://doi.org/10.1029/94RG01872

Large, W. G., & Yeager, S. G. (2009). The global climatology of an interannually varying air–sea flux data set. *Climate Dynamics*, *33*(2), 341–364. https://doi.org/10.1007/s00382-008-0441-3

Locarnini, R. A., Mishonov, A. V., Baranova, O. K., Boyer, T. P., Zweng, M. M., Garcia, H. E., et al. (2018). World ocean atlas 2018, volume 1: Temperature [Dataset]. *Silver Spring, MD, USA: NOAA National Centers for Environmental Information*. (Global ocean temperature climatology on standard depth levels from in-situ profile data; monthly fields regridded to CESM tx1_4 grid for use in model evaluation). https://doi.org/10.25921/X0Z1-7X04

Mak, J., Maddison, J. R., Marshall, D. P., Ruan, X., Wang, Y., & Yeow, L. (2023). Scale-awareness in an eddy energy constrained mesoscale eddy parameterization. *Journal of Advances in Modeling Earth Systems*, *15*(12), e2023MS003886. https://doi.org/10.1029/2023MS003886

Marques, G. M., Loose, N., Yankovsky, E., Steinberg, J. M., Chang, C.-Y., Bhamidipati, N., et al. (2022). NeverWorld2: An idealized model hierarchy to investigate ocean mesoscale eddies across resolutions. *Geoscientific Model Development*, *15*(17), 6567–6579. https://doi.org/10.5194/gmd-15-6567-2022

Marshall, J., Scott, J. R., Romanou, A., Kelley, M., & Leboissetier, A. (2017). The dependence of the ocean's MOC on mesoscale eddy diffusivities: A model study. *Ocean Modelling*, *111*, 1–8. https://doi.org/10.1016/j.ocemod.2017.01.001

Redi, M. H. (1982). Oceanic isopycnal mixing by coordinate rotation. *Journal of Physical Oceanography*, *12*(10), 1154–1158. https://doi.org/10.1175/1520-0485(1982)012⟨1154:OIMBCR⟩2.0.CO;2

Shea, D., Hurrell, J., & Phillips, A. (2020). Merged Hadley–OI sea surface temperature and sea ice concentration, version 1.0 [Dataset]. *UCAR/NCAR-DASH Repository*. (Monthly mean SST and sea ice concentration developed for CAM/AMIP boundary forcing; regridded fields used in CESM/MOM6 simulations). https://doi.org/10.5065/r33v-sv91

Shutts, G. (2005). A kinetic energy backscatter algorithm for use in ensemble prediction systems. *Quarterly Journal of the Royal Meteorological Society*, *131*(612), 3079–3102. https://doi.org/10.1256/qj.04.106

Solomon, H. (1971). On the representation of isentropic mixing in ocean circulation models. *Journal of Physical Oceanography*, *1*(3), 233–234. https://doi.org/10.1175/1520-0485(1971)001⟨0233:OTROIM⟩2.0.CO;2

Tsujino, H., Urakawa, S., Nakano, H., Small, R. J., Kim, W. M., Yeager, S. G., et al. (2018). JRA-55 based surface dataset for driving ocean–sea-ice models (JRA55-do). *Ocean Modelling*, *130*, 79–139. https://doi.org/10.1016/j.ocemod.2018.07.002

Yankovsky, E., Bachman, S., Smith, K. S., & Zanna, L. (2024). Vertical structure and energetic constraints for a backscatter parameterization of ocean mesoscale eddies. *Journal of Advances in Modeling Earth Systems*, *16*(7), e2023MS004093. https://doi.org/10.1029/2023MS004093

Yankovsky, E., Zanna, L., & Smith, K. S. (2022). Influences of mesoscale ocean eddies on flow vertical structure in a resolution-based model hierarchy. *Journal of Advances in Modeling Earth Systems*, *14*(11), e2022MS003203. https://doi.org/10.1029/2022MS003203

Yassin, H. (2025). houssamyassin/mom6-analysis: V1.0.0 [Software]. *Zenodo*. https://doi.org/10.5281/zenodo.17901066

Zhang, W., Griffies, S. M., Hallberg, R. W., Kuo, Y.-H., & Wolfe, C. L. P. (2024). The role of surface potential vorticity in the vertical structure of mesoscale eddies in wind-driven ocean circulations. *Journal of Physical Oceanography*, *54*(6), 1243–1266. https://doi.org/10.1175/JPO-D-23-0203.1